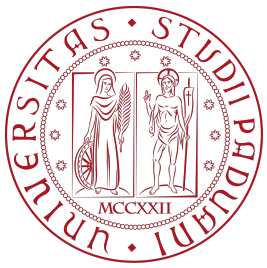

UNIVERSITÀ DEGLI STUDI DI PADOVA

Dipartimento di Fisica e Astronomia "Galileo Galilei"

Corso di Laurea in Fisica

Tesi di Laurea

Misura dei tempi di vita medi di stati nucleari eccitati popolati nella reazione ^{26}Mg + ^{238}U utilizzando la tecnica DSAM con lo spettrometro AGATA

Measurement of the lifetimes of nuclear excited states populated in the ^{26}Mg + ^{238}U reaction using DSAM technique with the AGATA spectrometer

Relatore

Prof. Francesco Recchia

Correlatore

Dr. Pablo Aguilera Jorquera

Laureando

Matteo Morgante

Anno Accademico 2023/2024

Abstract

In the region near the N=20 shell closure for neutron-rich nuclei, the lowest energy states are dominated by intruder configurations, in which some neutrons are excited across the shell gap. Nucleon-nucleon correlations and shell evolution lead to a progressive reduction of the sd-fp gap, lowering the energy of intruder states, until they become ground states, in an area called Island of Inversion. To get information on the structure of a nucleus in a specific excited state, it is useful to measure its lifetime. Being related to the reduced gamma transition probability, it may give an indirect description of the wave function associated with the state. This thesis is a preliminary analysis of an experiment that aims to study the spectra and obtain lifetime measurements of lower excited states in ^{27}Mg and ^{28}Mg, nuclei located near the western shore of the Island of Inversion. The states of interest were populated in multi-nucleon transfer reactions, using an accelerated ^{26}Mg beam on a ^{238}U target. The AGATA tracking array was used in coincidence with the PRISMA magnetic spectrometer, to detect gamma rays and associate them to the isotope that emitted them. Lifetimes are extracted from gamma spectra using the Doppler-Shift Attenuation Method, by comparing experimental peak shapes with those produced by Monte Carlo simulations, developed with `GEANT4`.

Nella regione vicina alla chiusura di shell a N=20 per nuclei ricchi di neutroni i primi stati nucleari eccitati risultano dominati da configurazioni "intruder", in cui alcuni neutroni sono eccitati a orbitali oltre lo shell gap. Man mano che ci si allontana dalla valle di stabilità, correlazioni nucleone-nucleone e deformazioni collettive portano ad una progressiva riduzione del gap tra shell sd e fp, abbassando in energia le configurazioni anomale, finché non diventano lo stato fondamentale in quella che viene chiamata Isola di Inversione. Per ricavare informazioni sulla struttura di uno stato nucleare, risulta utile misurarne il tempo di vita medio che, essendo legato alla probabilità di transizione gamma, può fornire indirettamente una descrizione della funzione d'onda relativa allo stato stesso. In questa tesi si fornisce un'analisi preliminare di un esperimento volto a indagare lo spettro e a misurare i tempi di vita medi dei primi stati eccitati di ^{27}Mg *e* ^{28}Mg*, nuclei prossimi ai limiti dell'Isola di Inversione. Gli stati oggetto di studio sono stati popolati tramite reazioni di trasferimento con fasci accelerati di* ^{26}Mg *su un bersaglio di* ^{238}U*. Per il tracciamento dei raggi gamma si è utilizzato l'array di rivelatori AGATA (Advanced Gamma Tracking Array) accoppiato allo spettrometro magnetico PRISMA per la selezione evento per evento degli isotopi di interesse. La misura dei tempi di vita medi è stata effettuata con il cosiddetto Doppler-Shift Attenuation Method, confrontando la forma dei picchi negli spettri gamma ottenuti nell'esperimento con quelli prodotti da simulazioni Monte Carlo realizzate con il software GEANT4.*

Contents

Chapter 1

Introduction

Atomic nuclei are complex many-body systems composed of strongly interacting neutrons and protons. The nature of the particles involved and the strong nuclear forces that keep them together make these systems particularly challenging to study. Apart from the collective properties that could be expected, nuclei also exhibit trends that are better explained by an independent particle behavior. The major evidence is the existence of particularly stable configurations for nuclei containing specific numbers of protons or neutrons, the so-called *magic numbers* (2, 8, 20, 28, 50, 82, 126) (Figure 1.1).

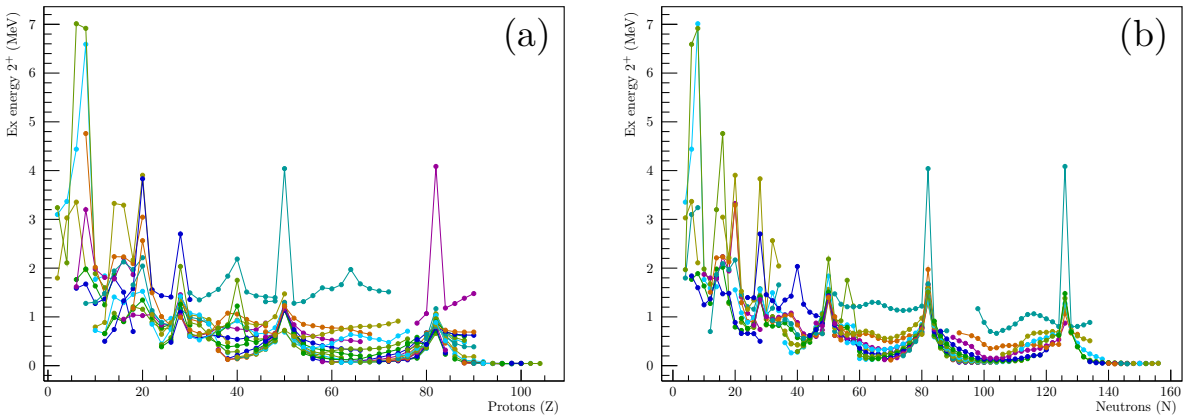

Figure 1.1: Evolution of the first 2^+ excited state energy in even-even nuclei, grouped by isotonic chains **(a)** and by isotopic chains **(b)**: the peaks correspond to magic numbers of protons and neutrons. Data from [1].

1.1 The nuclear Shell Model

To account for all these properties, many theoretical approaches have been put forward over time. One of the most successful is the *shell model*, first developed by Maria Göppert Mayer and Hans Jensen in 1949 [2, 3]. Originally, it was conceived as an independent particle model, in which nucleons are assumed to be confined in a spherical mean-field potential consisting of a central term (usually harmonic oscillator or Woods-Saxon potential) and a strong spin-orbit coupling

$$U_{\mathrm{mf}}(r_i) = V(r_i) + k(r_i)\vec{L}_i \cdot \vec{S}_i \tag{1.1}$$

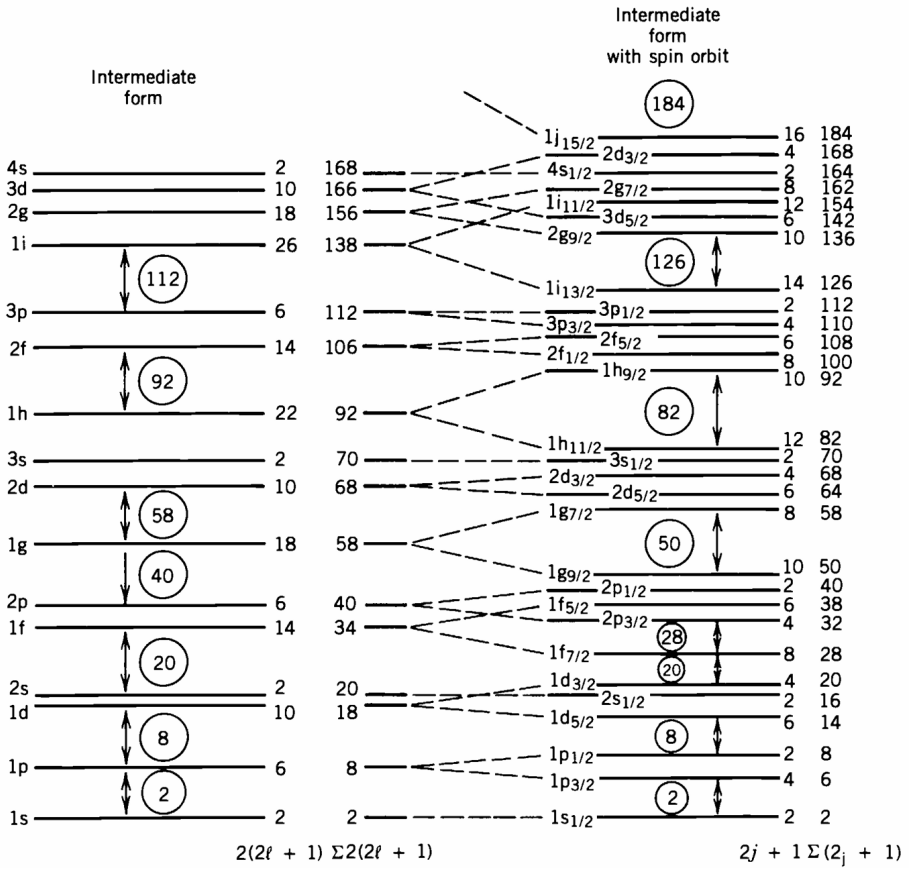

Figure 1.2: Level scheme obtained from the independent particle shell model. On the left the partial version with a Woods-Saxon potential, on the right the levels obtained by adding the spin-orbit term of Göppert Mayer. With this term the magic numbers are correctly reproduced. From [4].

Protons and neutrons are then distributed in shells with energy levels obtained from the diagonalization of the single particle Hamiltonian, the ground state obtained by filling the lowest orbitals first. The shell closures obtained with this approach successfully reproduce all the magic numbers experimentally observed (Figure 1.2). However, this independent particle approach falls short when trying to describe excited states and nuclei located far from the shell closures.

In the last decades, thanks to the development of massive computational frameworks, this model has been extended to account for the effective interactions between nucleons, treating them as perturbations to the spherical mean field. The new version, named interactive shell model, aims to find the eigenvectors of the nuclear Hamiltonian completed with a residual two-body interaction term:

$$H = \sum_{i=1}^{A} \left[\frac{p_i^2}{2m_i} + U_{\mathrm{mf}}(r_i) \right] + \frac{1}{2} \sum_{i,j=1}^{A} V_{ij} = \sum_{i=1}^{A} h_i + H^{\mathrm{res}} \tag{1.2}$$

The research is conducted among linear combinations of single-particle configurations $|\phi_I\rangle$ and basically consists of the diagonalization of the matrix $\langle \phi_I | H | \phi_{I'} \rangle$. This problem remains however difficult to treat, because of the high dimensionality of the matrix. In practice, this kind of computation can be achieved only by allowing only a small number of nucleons to interact (the *valence* particles) and, at the same time, limiting the possible single-particle states that can be occupied (the *valence* space). In this way, different *valence spaces* and *effective Hamiltonians* are defined and adapted to get reasonable descriptions of nuclei in specific regions of the chart [5].

A fundamental tool that provides the information to construct these Hamiltonians and allows to check their predictions is represented by the experimental measurement of lifetimes of nuclear states. From these observables, in fact, direct information on the structure of nuclei can be extracted.

The lifetime of a state with spin J_i that decays by an electromagnetic transition to a J_f state is given by

$$\tau^{-1}(\sigma L, J_\mathrm{i} \to J_\mathrm{f}) = \frac{2}{\hbar\varepsilon_0}\frac{L+1}{L[(2L+1)!!]^2}\left(\frac{E_\gamma}{\hbar c}\right)^{2L+1} B(\sigma L, J_\mathrm{i} \to J_\mathrm{f}) \tag{1.3}$$

where $\sigma \in (E, M)$ indicates the type of the transition, electric or magnetic, and L its multipolarity. The quantity $B(\sigma L, J_\mathrm{i} \to J_\mathrm{f})$ is called reduced transition probability and is related to the wave functions of the states involved in the decay and to the multipolar electromagnetic operator $\mathcal{O}(\sigma L)$:

$$B(\sigma L, J_\mathrm{i} \to J_\mathrm{f}) = \frac{1}{2J_\mathrm{i}+1} \left|\left\langle J_\mathrm{f}\right| \mathcal{O}(\sigma L) \left|J_\mathrm{i}\right\rangle\right|^2 \tag{1.4}$$

This equation implies that from the reduced transition probability it is possible to quantify the overlap between the wave functions of initial and final states or, equivalently, to know the degree of similarity between the two nuclear configurations.

1.2 The Island of Inversion at N=20

As a consequence of the residual interaction between nucleons, it may happen that the ground state configuration experimentally observed is not the one that could be expected by applying the usual shell-filling pattern. In these cases the most stable states are deformed configurations with two or more nucleons located on higher energy levels, leaving holes in the shell structure. The dominance of such states, called *intruders*, has been observed in the neutron-rich regions on the chart located near the semi-magic shell closures at N=20, 28, 40. These regions are called *Islands of Inversion*, because of the subversion of the expected state order: their study is of fundamental importance to grasp a better understanding of the interactions between nucleons and of their impact on several spectroscopic properties.

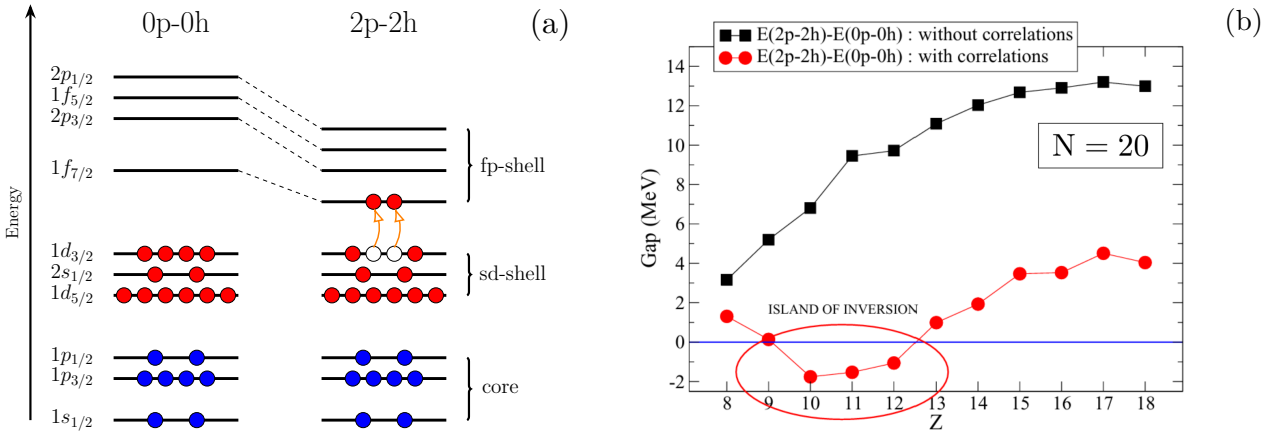

Figure 1.3: **(a)** Shell structure of neutrons for ^{32}Mg. On the left the normal configuration with a full *sd* shell. On the right the intruder 2 particle - 2 hole state, with two neutrons promoted to the *fp* shell, helped by the reduction of the energy gap. Adapted from [6].
(b) Energy gap between the normal and the 2h-2p configurations for different Z values at $N = 20$, calculated with the SDPF-U-MIX interaction by including or not the correlations between nucleons. Correlations lower the gap, that becomes negative in the IOI. Adapted from [7].

A major example is represented by the Island at N=20, located around ^{32}Mg. In this nucleus, the main component of the ground state is a 2-particle 2-hole configuration, with two neutrons that populate the *fp* shell instead of closing the lower *sd* shell, a behavior that would be expected for a true semi-magical system (Figure 1.3-(a)). Intruder states are dominant also in nearby nuclei, thus forming the island. Going through the isotonic chain at N=20 from the valley of stability, or in a similar way, following the Mg isotopes horizontally on the chart, a progressive reduction of the energy gap between the *sd* and the *fp* shells has been observed. This phenomenon, combined with correlations and deformation effects, leads to an enhanced competitiveness of intruder bands over normal spherical configurations, which eventually is so pronounced that an intruder becomes the ground state [8].

In recent years, many theoretical studies have been conducted to understand the shell evolution in the island with state-of-the-art Shell Model calculations: for example, a merging between this and the island at the next shell gap at N=28 was established by analyzing the Z=12 isotopic chain [7]. However, experimental information remains quite scarce and the definition of the "eastern" shore of the island, the border facing the valley of stability, is still not clear. Understanding the intrusive or normal nature of the different excited states in the nuclei near the island represents nowadays an interesting case of study.

1.3 Outline and objectives of the thesis

This work represents a preliminary analysis of experiment 23.068 aimed at exploring the transition into the Island of Inversion towards N=20 from the Z=12 isotopic chain, performed at the Legnaro National Laboratories (LNL) in June 2024. In this experiment, the low-lying states of isotopes in the region between the β valley of stability and the Island of Inversion, highlighted in figure 1.4, were populated with multi-nucleon transfer reactions using a beam of ^{26}Mg impinged on a neutron-rich ^{238}U target. The beam-like ions produced were detected using the PRISMA [9] magnetic spectrometer, while γ-rays emitted coincidentally were tracked by AGATA [10], the Advanced GAmma Tracking Array. Such experiment is part of a wider campaign of three proposals, aimed at conducting a systematic investigation on different properties (collective structure, presence of intruder states among the main ones) of isotopes in the region towards the Island of Inversion at $N = 20$. In the different stages of the campaign, similar multi-nuclear reactions are studied, using the same experimental setup and changing only the beam: ^{22}Ne for the first step, already completed during 2022, and ^{30}Si for the last one, to be done in the next years.

The thesis focuses on the analysis of the γ-ray spectra of ^{27}Mg and ^{28}Mg, two of the channels populated in this reaction. Previous measurements of the lifetimes of their excited states show that they mostly lie in the range from ≈ 10 fs to ≈ 1 ps (see [11, 12, 13] for ^{27}Mg and [14, 15] for ^{28}Mg). To get access to this range, a series of techniques that exploit the Doppler shift in energy of γ-rays emitted in nuclear de-excitation has been developed. The main ones are the Doppler Shift Attenuation Method (DSAM), which is effective in a $50 \div 800$ fs range, and the Recoil Distance Doppler Shift (RDDS), mostly effective for longer lifetimes ($\sim 1 \div 100$ ps). The focus will be on the DSAM technique, which is the one implemented in the experiment analyzed. This method consists in optimizing the energy loss of recoiling ions after the reaction, often by attaching a foil of degrading material after the target. Since the Doppler effect heavily depends on the ions' velocity, the detected energies of γ-rays emitted inside or outside the degrader are different. Thus by analyzing γ spectra, it is possible to extract

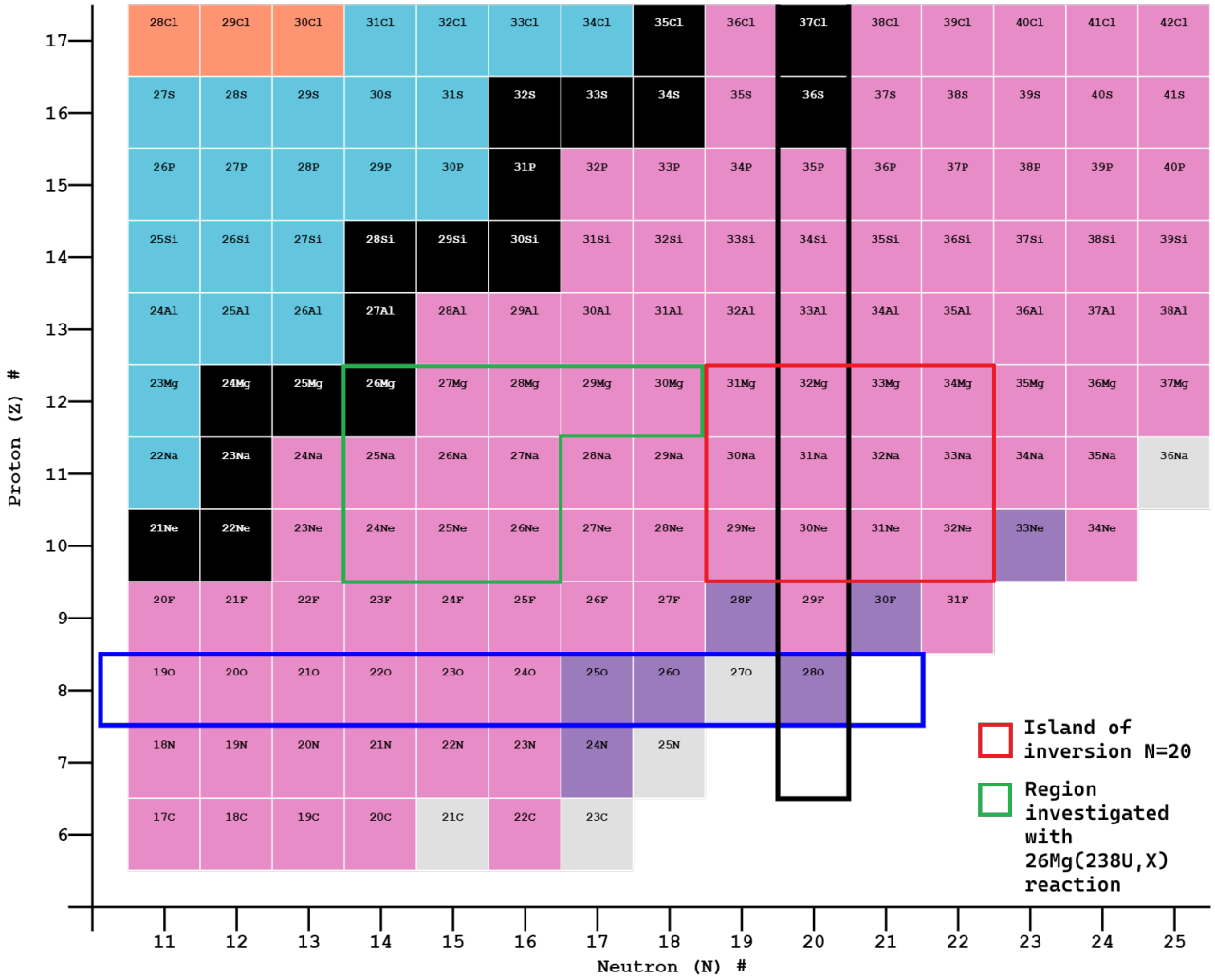

Figure 1.4: The Island of Inversion at N=20 on the nuclide chart and the region explored in the experiment object of the thesis. Adapted from [1].

information on where the decays take place or, equivalently, on the lifetime of a certain state. Actual measurements are extracted via a comparison between experimental peaks in the γ-ray spectra and the ones generated by Monte Carlo simulations implemented within the `GEANT4` framework, optimized to faithfully reproduce both reaction physics and experimental conditions. The aim of the thesis is to calibrate the simulation and investigate whether this methodology produces accurate results. To accomplish this, the lifetime of appropriately selected excited states in the spectra of the two nuclei of interest will be calculated and compared with the values present in the literature.

The work is organized as follows. In the second chapter, an essential overview of the detectors used in the experiment is given, with a focus on details that are useful for the subsequent analysis and an explanation of the DSAM technique employed for the lifetime estimation. Following this, in the third chapter the procedures implemented to analyze the data and optimize the `GEANT4` simulation are explained in detail. The results obtained for the selected lifetimes will be presented and thoroughly discussed. Finally, in the fourth and last chapter a summary of the work and the conclusions drawn from the results are presented.

Chapter 2

The experimental setup

In this chapter details about the setup, the detectors, and the methodologies adopted in the experiment object of the thesis will be given. In the experiment, performed at the Legnaro National Laboratories (LNL) in June 2024, a stable ^{26}Mg beam was accelerated at 200 MeV by the Tandem-ALPI accelerator complex. The beam was directed on a 1 mg/cm^2 thick ^{238}U target, placed perpendicularly to the beam-line. The target was backed with a 5 mg/cm^2 degrader foil of ^{93}Nb, specifically attached to perform lifetime measurements using the DSAM technique (sec. 2.3). The beam-like ions produced in the multi-nuclear transfer reactions were detected by the PRISMA magnetic spectrometer (sec. 2.1), positioned to form a 50° angle with the beam trajectory. This angle was chosen to maximize the cross sections of ^{26,27,28,29}Mg isotopes. The gamma rays emitted by the reaction products were instead detected by the AGATA spectrometer (sec. 2.2), triggered by PRISMA.

2.1 The magnetic spectrometer PRISMA

PRISMA is a large acceptance magnetic spectrometer constructed at LNL and designed for the heavy-ion beams with $E_{\text{beam}} = 5 \div 10$ MeV/A of the Tandem-ALPI-PIAVE accelerator complex [9]. In this experiment it serves for the A and Z identification of ions produced in the reaction. It reconstructs their trajectories and measures their velocities, information needed to apply the Doppler correction to γ-ray energies detected by AGATA. The spectrometer covers a 80 msr solid angle, corresponding to $\Delta\theta \approx 12°$ acceptance in the horizontal plane and $\Delta\phi \approx 22°$ in the vertical plane. It has a large momentum acceptance ($\pm 10\%$) and a good mass resolution of 1/300 via ToF measurements [9]. PRISMA is characterized by a very simple optical design, consisting of a quadrupole singlet (50 cm long, with 30 cm diameter) that focuses particle trajectories in the vertical plane, followed by a dipole characterized by a 120 cm radius of curvature and a 60° deflection angle. It is composed of three detectors, namely the Micro-Channel-Plate (MCP) [16], the Multi-Wire Parallel-Plate Avalanche Counter (MWPPAC) [17], and the Ionization Chamber (IC).

A schematic representation of the apparatus is shown in figure 2.1. The MCP is the entrance detector: positioned 25 cm after the target, it records the two-dimensional position (x_0, y_0) and time t_0 at which reaction fragments enter PRISMA. Then, ions pass through the quadrupole element and are deviated by the dipole depending on their charge and mass. After that, particles reach the MWPPAC, which records a second time signal t_1 and measures again their position (x_1, y_1). From these measurements, trajectories, times of flight (ToF) and particle masses are later reconstructed via software on an

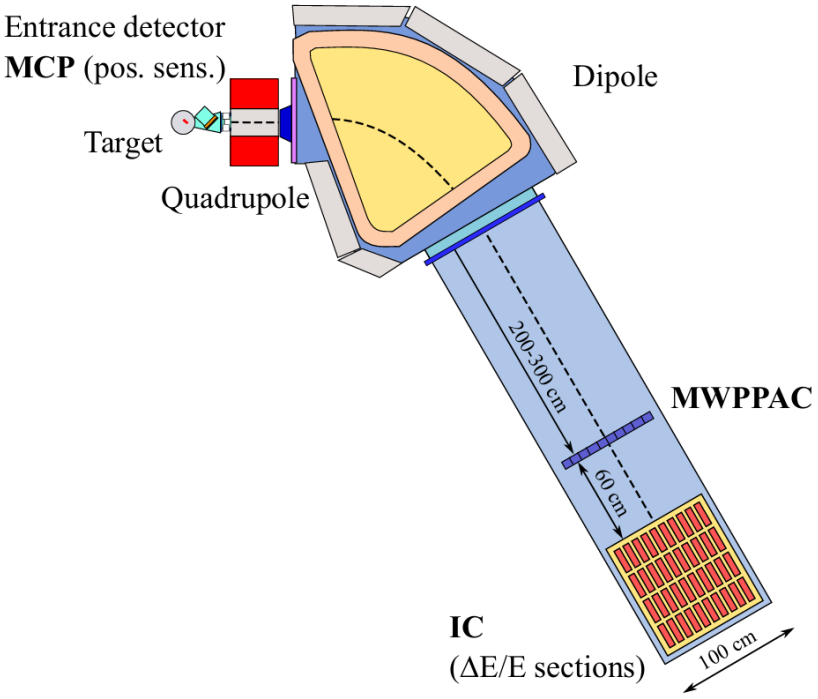

Figure 2.1: Scheme representing the main elements of the PRISMA magnetic spectrometer. From [18].

event-per-event basis. At the end, ions are stopped in the Ionization Chamber, which consists of a large active volume filled with low pressure ($\approx$ 55 mbar) carbon tetrafluoride (CF_4), segmented into 40 different sections that provide independent measurements of the energy lost by particles in each of them. From the different ΔE values, the ion charge Z is then identified using the $\Delta E - E$ technique, based on the Bethe-Bloch expression for the stopping power of heavy charged particles.

2.2 The gamma ray tracking spectrometer AGATA

AGATA (Advanced GAmma Tracking Array) [10] is a European project aimed at developing a new generation, high-resolution γ-ray spectrometer. In its final configuration, the array will be composed of 180 High-Purity Germanium (HPGe) detectors arranged in a honeycomb structure to cover the maximum solid angle of 4π around the target. Since 2022 it has been operating at LNL, where it has been coupled with PRISMA and several other ancillary devices [19]. For the experiment analyzed in this work, a total of 12 clusters of detectors were used, positioned to cover a solid angle of $\approx 1\pi$ (see figure 2.2 for the operative clusters and 2.3-(a) for a scheme of the total experimental setup).

The detectors are based on encapsulated n-type High-Purity Germanium crystals, that are 90 mm long and tapered in slightly asymmetrical hexagonal shapes of three different types [10]. They are assembled in groups of 3, called AGATA Triple Clusters (ATC), that share the same cryostat, needed to cool them to an operative temperature of 80 K. The main feature of these crystals, that distinguishes AGATA from other γ spectrometers, is their high electrical segmentation. Each crystal is segmented into 6 rings, which are also divided radially into 6 parts, as shown in figure 2.2: this characteristic gives the possibility to reconstruct the trajectories followed by γ-rays inside the detector.

Whenever a photon interacts with the detector, mainly via photoelectric effect, Compton scattering or pair production, a fraction (or all) of its energy is deposited in the crystal; consequently, an electric

signal is induced in some of its segments. By analyzing the shape of such signals with specific Pulse Shape Analysis (PSA) algorithms, the exact position of the interaction can be extracted with a good resolution. A sophisticated tracking software then analyzes all points of interaction within a reasonable time frame to identify which refer to the same photon, and to find their temporal order and their typology. Thanks to the high number of crystals, their positioning and segmentation, the path followed by γ-rays in the detector can be reconstructed very efficiently. In particular, the identification of the first interaction point is of notable importance, because it results in a more precise Doppler correction to the measured γ-ray energies and, ultimately, in a better energy resolution of Doppler corrected spectra, due to a reduction of the so-called *Doppler broadening* of energy peaks. A further insight on the AGATA data pre-processing and on the tracking algorithms implemented can be found in [20].

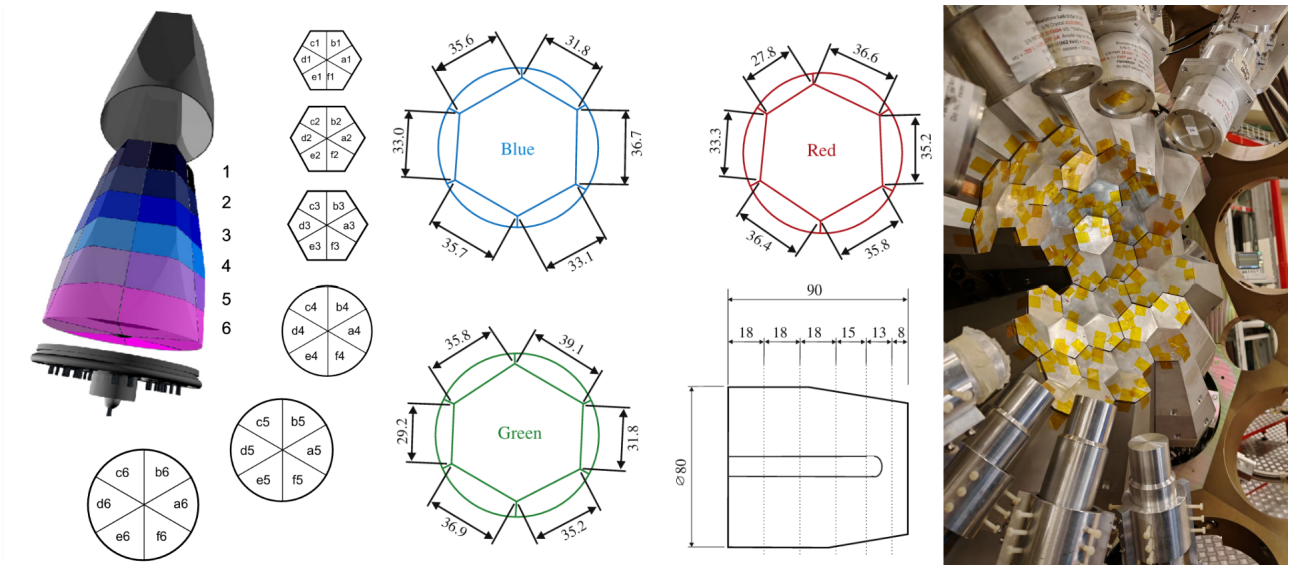

Figure 2.2: Geometry and segmentation of AGATA HPGe crystals [10]. In each triple cluster, there are a blue, a green and a red crystal respectively, all are divided in 36 segments. On the right, AGATA in the configuration of the experiment, with 12 operative ATCs.

2.3 The Doppler Shift Attenuation Method (DSAM)

The Doppler Shift Attenuation Method is a technique developed to measure lifetimes within a range going from tens of femtoseconds to a picosecond. The method consists of adopting a specially designed two-layer target system: the first layer acts as the proper target where the reaction takes place, the second one is a thicker foil of material called *degrader*, that slows down the products of the reaction. In this experiment, the target is made of ^{238}U and is 1 mg/cm^2 thick while the backing is a 5 mg/cm^2 thick layer of ^{93}Nb. A schematic representation of the setup adopted in the experiment and of the positioning of the detectors is shown in figure 2.3-(a).

Gamma ray energies measured by AGATA detectors are affected by a Doppler shift, that depends both on the emitting ion velocity and on the detection angle. The measured energy E_γ is related to the actual photon energy E_γ^0 by this relation:

$$E_\gamma^{\text{meas}}(\beta,\theta) = E_\gamma^0 \left[\frac{\sqrt{1-\beta^2}}{1-\beta\cos\theta}\right] \equiv E_\gamma^0\, D(\beta,\theta) \tag{2.1}$$

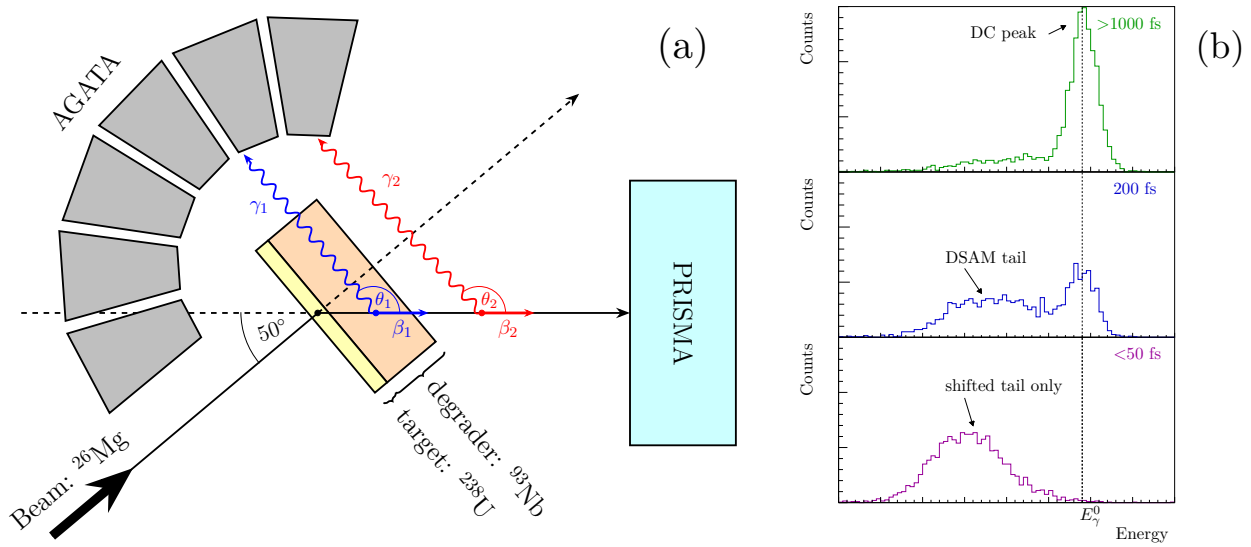

Figure 2.3: **(a)** Diagram of the experimental setup and DSAM implementation (not in scale). The target + degrader system is placed perpendicular to the beam; PRISMA is placed to detect beam-like ions forming a 50° angle with the beam trajectory, AGATA covers the backwards angles respect to the recoiling ion. Two gammas, emitted inside (blue) and outside (red) the degrader are highlighted. **(b)** Simulated line-shape spectra for different lifetimes. The different contributions of the Doppler corrected peak centered at E_γ^0 and of the DSAM tail are evident.

where $\beta = v/c$ is the ratio of the emitting ion velocity to the speed of light and θ is the angle between the ion trajectory and the γ-ray. While the angle of detection is estimated with high accuracy and resolution by AGATA, the velocity of recoiling ions is directly measured by PRISMA only after they have passed through the degrader. This implies that the Doppler correction that can be applied to the γ-ray energy spectra is one that makes use of this measure of β, which does not depend on where the single photons were emitted. Since the γ-ray emission is statistical and the slowdown in the degrader is continuous, the energy spectrum resulting from the Doppler correction with the final β_f is a continuous distribution that strongly depends on where the decays happened.

If the lifetime of the state is much larger than the time used by the ion to pass through the degrader, then the majority of γ emissions take place out of the foil. For these emissions, the emitter β corresponds to the one measured by PRISMA and used for the Doppler correction, so the expected distribution is a Gaussian peak centered around the correct E_γ^0. Instead, if the lifetime is comparable with the time taken to go through the degrader, many decay events occur when the ion is slowing down inside the foil. This implies that for these γ-rays the Doppler shift applied is not correct: the corresponding distribution in the spectrum is then characterized by a reduced peak around E_γ^0 with a tail that accounts for the transitions that occurred in the degrader. The shorter the lifetime of a state, the more dominant the tail becomes: if all decays take place inside the medium, only the tail appears in the spectrum as a broad, shifted Gaussian peak (see figure 2.3-(b)).

In the configuration adopted in the experiment, with AGATA positioned to cover the backward angles with respect to the recoiled ions trajectory ($\theta > 90°$ in equation 2.1), the Doppler shift applied to photons emitted in the degrader is a systematic *under-correction*. This means that the values obtained for their energies are always lower than the correct ones, and that the DSAM tail consequently appears on the left of the E_γ^0 main peak. The extension of the tail is determined by the difference between the ion velocity right after the reaction β_i and the one measured by PRISMA β_f, difference that ultimately depends on the thickness of the degrader. An accurate measurement of lifetime via the analysis of

the spectrum line shape is possible if the tail is sufficiently broad, greater than the detector energy resolution. As it can be seen in figure 2.4 with an example of the ^{26}Mg(^{238}U,^{27} Mg) two-body reaction, numerical calculations of the kinematics show that the target-degrader thicknesses adopted in the experiment cause an overall reduction of approximately $\Delta\beta/\beta_{\mathrm{i}} = (\beta_{\mathrm{i}} - \beta_{\mathrm{f}})/\beta_{\mathrm{i}} = 11\%$ in the velocity of ions recoiling at 50°. This means that, after a Doppler correction by a factor $D(\beta_{\mathrm{f}}, \theta)$, gammas emitted immediately after the reaction appear in the energy spectrum at

$$E_\gamma^{\mathrm{DC}} = E_\gamma^{\mathrm{meas}} \frac{1}{D(\beta_{\mathrm{f}}, \theta)} = E_\gamma^0 \frac{D(\beta_{\mathrm{i}}, \theta)}{D(\beta_{\mathrm{f}}, \theta)} \approx E_\gamma^0 \cdot 0.99 \tag{2.2}$$

for γ-rays emitted at $\theta \approx 120°$. The DSAM tail extension thus varies along the spectrum and is approximately 1% of transition energy; this is sufficient to get a good sensitivity for γ-rays over 1 MeV.

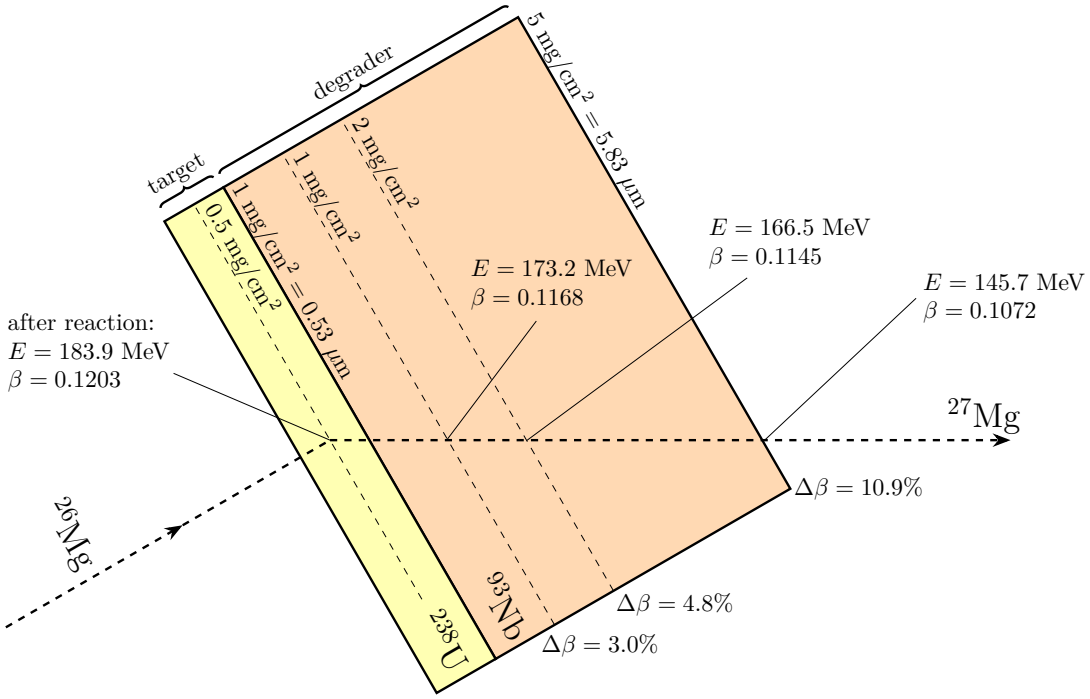

Figure 2.4: Kinematics of the ^{26}Mg(^{238}U,^{27} Mg) reaction. Values of the recoiling ^{27}Mg in different places inside the degrader are shown. Calculations carried out with the software LISE++ [21].

The lifetime of an excited state that decays with a specific γ transition is obtained by comparing line-shapes of the experimental spectrum with the one produced with Monte Carlo simulations adapted to mimic the experimental conditions. These simulations, performed using the `GEANT4` software, take into account all the factors relevant to the analysis: setup geometry, finite resolution of the detectors, angular distribution of the recoils, cinematic of the reaction and phenomena involved, level population and decays modes of the interested ions. Everything can be set to get an accurate reproduction of the experiment: after having optimized all other parameters, a set of simulations is conducted by only changing the lifetime of a state of interest. Then, final estimations are extracted via χ^2 comparisons with experimental peak-shapes.

Many sources of uncertainty and of systematic errors can affect the results obtained by implementing this methodology. Among the main ones, the limited knowledge of the population of energy levels in the reaction and the side feeding of the levels need to be mentioned.

Chapter 3

Data analysis and lifetime estimation

The analysis carried out on experimental data is presented in this chapter. It is worth to note here that all the spectra and histograms that will be presented and used in this work are not definitive and come from a partial and incomplete pre-processing analysis on raw data coming from AGATA and PRISMA. The experiment was conducted very recently and many advanced corrections and calculations may still be performed to get more precise and polished spectra. So all results obtained and reported here have to be considered preliminary.

In section 3.1 the aim is to reconstruct partial level schemes for ^{27}Mg and ^{28}Mg, highlighting observed transitions and energy levels populated in the experiment. In particular, levels whose lifetimes are feasible to be measured with the DSAM technique are selected. The following section (3.2) focuses on the methodology used to extract lifetime measurements from the simulations and how the simulations were prepared for the task. Finally, the specific results obtained for the selected levels are shown in detail (sec. 3.3).

3.1 Analysis of the gamma ray spectra

The first step needed to obtain lifetime measurements is represented by a preliminary analysis of the γ-ray spectra of the isotopes of interest. The aim is to identify visible peaks, associating them to known gamma transitions, and then to extract information on the population of the levels of interest, to finally construct a partial level scheme containing all the results. This kind of analysis is necessary to obtain a fine-tuning of simulations and to identify possible systematics that can affect final measurements.

In figures 3.1 and 3.2 Doppler corrected spectra of ^{27}Mg and ^{28}Mg resulting from preliminary data pre-processing are reported. The identification of lines is not trivial because of the possible shift in the energy of transitions related to levels with lifetimes in the DSAM sensitivity range. To address this difficulty, a fit has been performed on each peak to find its centroid, FWHM, and number of counts. such fits were conducted on a small region around the peak of interest, using a function constructed with a decaying exponential component for the background and a sum of two Gaussians with exponential tails for the two components (DSAM and DC) of each peak. Then, known γ-ray lines that could correspond to one of the centroids, eventually addressing the DSAM shift (always towards lower energies), were searched in the NNDC database [1].

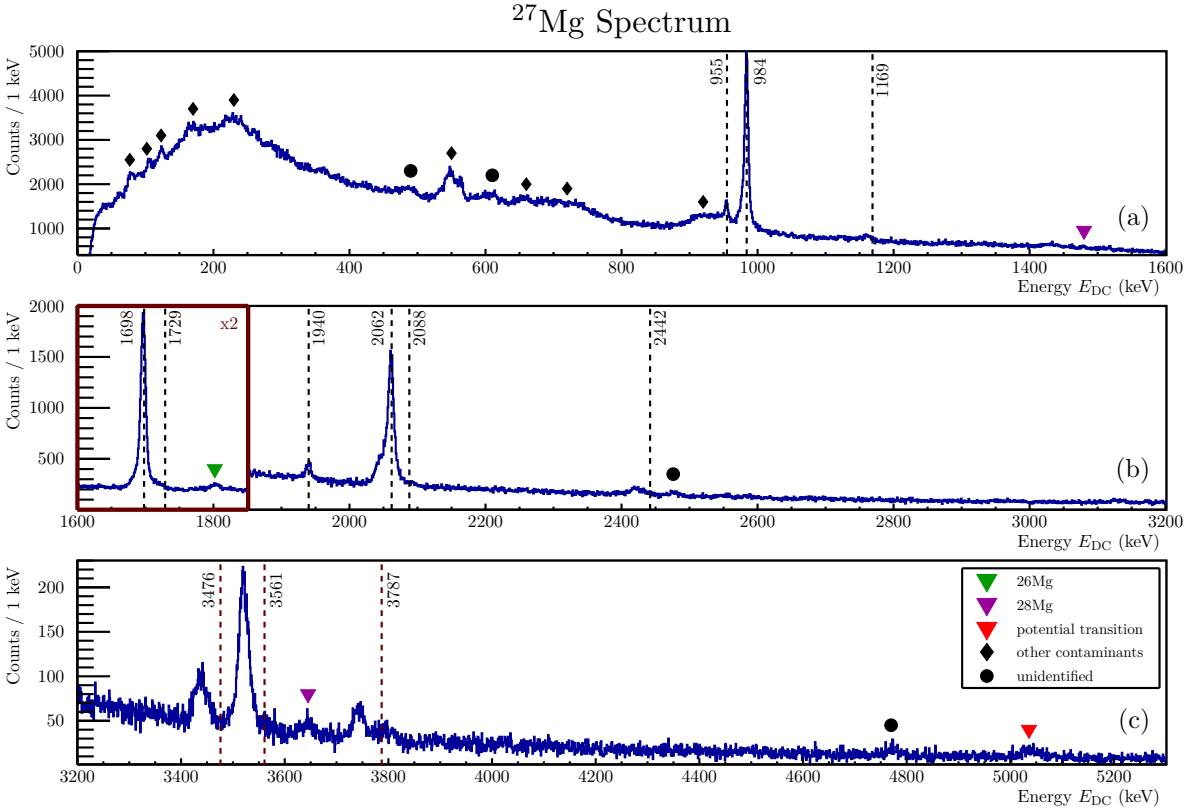

Figure 3.1: Doppler corrected spectrum of ^{27}Mg. Dashed lines correspond to known low-lying transitions in ^{27}Mg (data from [1]). Peaks not corresponding to known lines are marked as contaminants, possible new transitions or unidentified (see common legend in **(c)**).

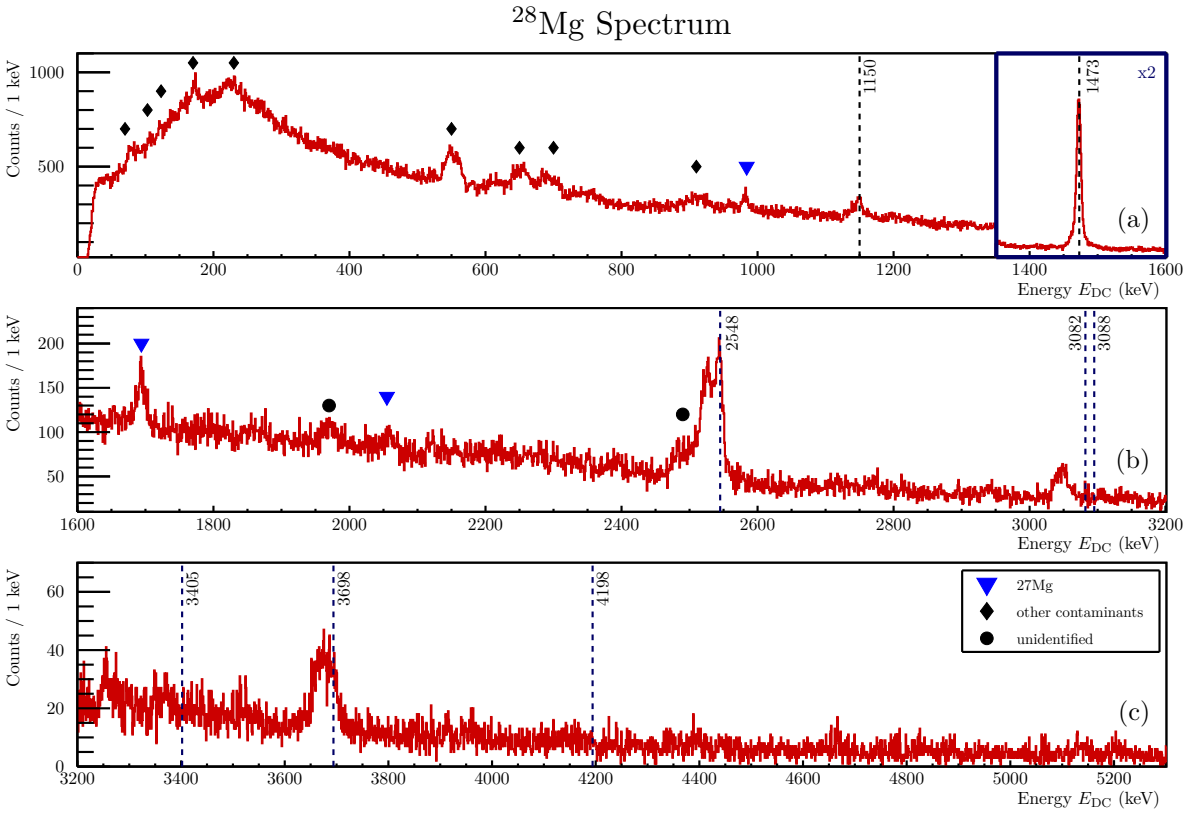

Figure 3.2: Doppler corrected spectrum of ^{28}Mg. Dashed lines correspond to known low-lying transitions in ^{28}Mg (data from [1]). Peaks not corresponding to known lines are marked as contaminants, possible new transitions or unidentified (see common legend in **(c)**).

To avoid false positive identifications, DC spectra of all Mg isotopes produced in the reaction have been compared, in order to find common trends and contaminants. The PRISMA analysis procedure to identify a recoiling ion mass is not immune to error, especially at this stage of the analysis; as a consequence a fraction of the gamma events could be assigned to the wrong spectrum. This implies that very intense transitions that are typical of a ^{A}Mg isotope could appear also in the spectra of near $^{A\pm1}$Mg as contaminant peaks. This kind of contamination is to be seen in both the analyzed spectra: in ^{27}Mg the 1808 keV transition from the first excited 2^+ to the ground state of ^{26}Mg and the equivalent 1473 keV transition in ^{28}Mg leave a trace; whereas in ^{28}Mg the 3 most intense transitions of ^{27}Mg are visible. Peaks present in all ^{A}Mg spectra with similar shapes are instead common contaminants related to other experimental components. The main ones are the 511 keV pair production peak (shifted by the Doppler correction to 550 keV), X-ray emissions of the target ^{238}U ($80 \div 100$ keV range), excitations of ^{73,74}Ge of AGATA detectors (609 keV) and ^{93}Nb in the degrader. Such contaminant peaks are mainly present in the $0 - 900$ keV region and can be better identified by observing the spectrum without Doppler correction, since they are correlated to photons emitted at rest.

As a cross-check to help in the level scheme construction, $\gamma - \gamma$ coincidences have also been analyzed, by gating on intense transitions that should be at the base of γ-ray cascades. In particular, gates on 984 keV and 1698 keV were applied in ^{27}Mg, on 1473 keV and 2442 keV in ^{28}Mg.

For each peak that was still not identified, $\gamma - \gamma$ coincidences have been searched with other lines to eventually find candidates for still unknown transitions. This process has given positive results for a peak centered at 5036 keV in the ^{27}Mg spectrum, highlighted with a red triangle in 3.1-(c): a clear coincidence with the transition at 984 keV can be observed by gating on the $5026 \div 5046$ keV energy interval, coincidence which is evident also in the opposite scenario, with a gate on the 984 keV peak, as shown in figure 3.3-(c) and (d). It is then possible that this 5036 keV peak could be the evidence of a hypothetical transition that connects the first $3/2^+$ excited level at 984 keV with another one located approximately between 6020 and 6100 keV. No known transition in ^{27}Mg lies within the $5030 \div 5100$ keV energy range; on the other hand there is one level, located at 6084(2) keV and found both in [11] and [22], that lies in the interval hypothesized before.

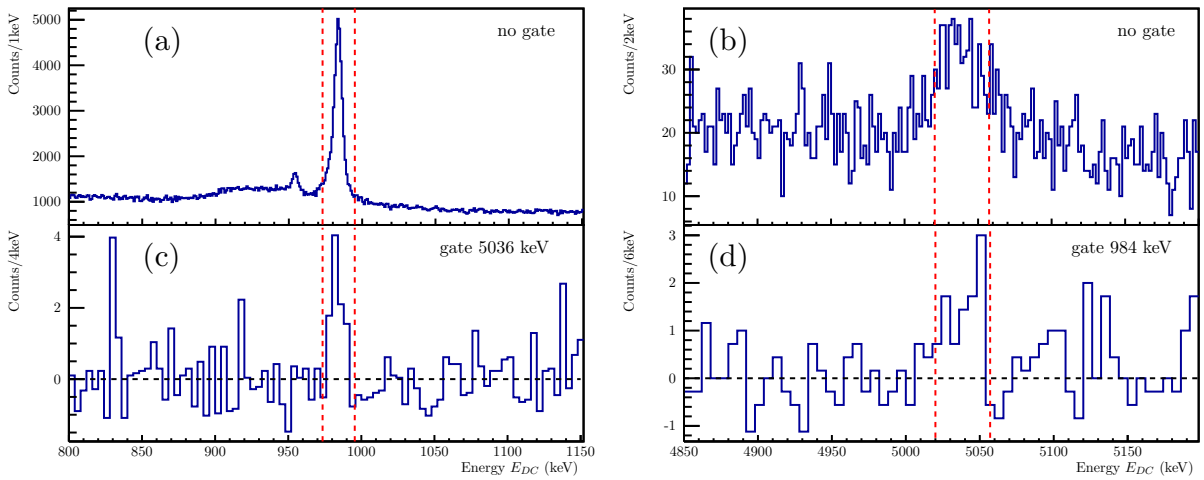

Figure 3.3: **(a)** ^{27}Mg spectrum: zoom on the $[800 - 1150]$ keV energy interval.
(b) Same for $[4850 - 5200]$ keV energy range. The peak at 5036 keV is evident.
(c) Spectrum gated on 5036 keV (the gate region is highlighted between red lines in **(b)**) the 984 keV peak is still visible.
(d) Spectrum gated on 984 keV (gate interval between red lines in **(a)**) in the 5 MeV energy region.

The exact transition energy value cannot be easily extracted, because it is not possible to know if the peak is shifted by the Doppler correction or not. However, since all measured lifetimes for states with excitation energy higher than 5 MeV in even-odd nuclei around ^{27}Mg are lower than 100 fs (see [1]), one could reasonably state that the lifetime of this transition initial state would be no different. This would imply a totally shifted peak and, considering a Doppler correction of about 1%, a transition of approximately $5080 \div 5090$ keV, energy eventually compatible with a 6084(2) keV initial state.

A first estimate of relative intensities for all transitions was finally calculated from the number of counts in each peaks, by keeping into account the dependence on energy of AGATA detectors efficiency, reported in figure 3.4. The intensity of a transition γ relative to a reference γ' was evaluated as follows:

$$I_{\text{rel}} = \frac{N_\gamma \cdot \varepsilon(E_\gamma)}{N_{\gamma'} \cdot \varepsilon(E_{\gamma'})} \tag{3.1}$$

where N_γ is the measured number of counts in the peak and $\varepsilon(E_\gamma)$ is the efficiency at its energy. Relative intensities are useful for level scheme reconstruction, since for each excited level the total feeding from other transitions must be lower than the total intensity of outgoing γ-rays.

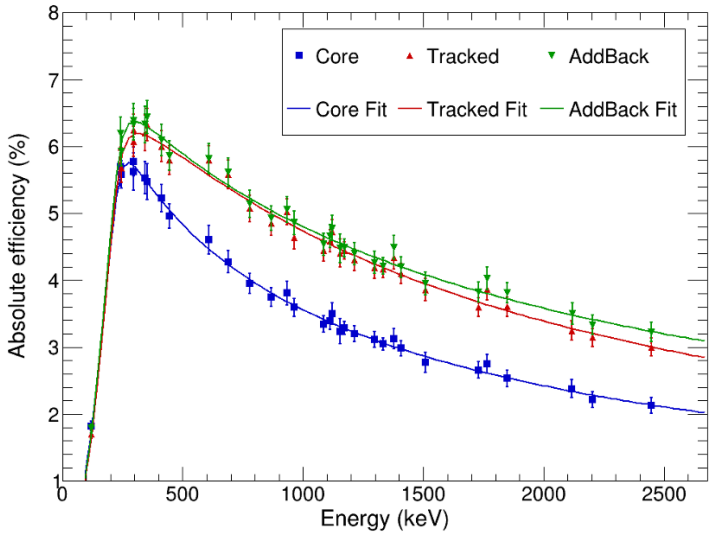

Figure 3.4: AGATA efficiency curves. Calibration on ^{60}Co source executed in 2022 with a similar configuration (34 active detectors, nominal position) [23]. Data are fitted with the RadWare function [24]. Different curves refer to different modes of data analysis: the red *tracked* curve, that refers to energies reconstructed by the tracking algorithm as happens for the spectra analyzed here, was the one used to calculate intensities.

3.1.1 Partial level scheme reconstruction of ^{27}Mg and ^{28}Mg

Gathering the information obtained from the spectra, partial level schemes are constructed for the two isotopes of interest (fig 3.5 for ^{27}Mg and 3.6 for ^{28}Mg). Spins and parities of the levels are assigned according to the ones reported on the NNDC database [1], when available. The width of the arrows that represent different transitions is proportional to the measured intensity, obtained with the procedure explained in the previous paragraph. For ^{27}Mg all intensities are normalized with respect to the 984 keV $3/2^+ \rightarrow 1/2^+$ transition; whereas for ^{28}Mg they are relative to the 1473 keV transition, always going from the first excited to the ground state. Dashed arrows refer to peaks with unclear transition designations. This is the case when low resolution in energy, combined with the presence of Doppler

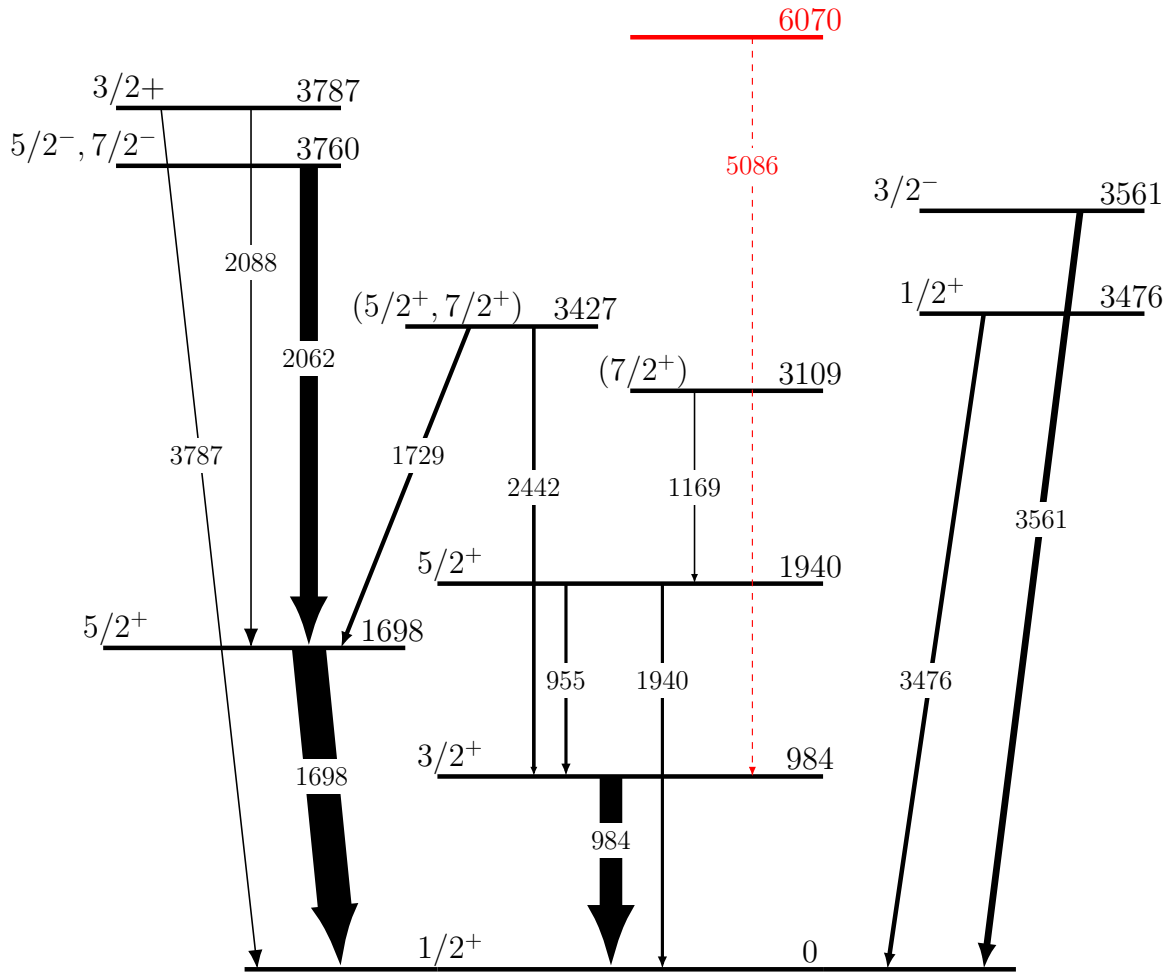

Figure 3.5: Reconstructed level scheme of ^{27}Mg. The dashed red arrow refers to the candidate unknown transition.

Energy levels		Previous τ measurements			Transitions				
E_i keV	J_i^π	τ [11] ps	τ [13] ps	τ [12] ps	E_f keV	J_f^π	E_γ keV	I_γ %	Br %
984	$3/2^+$		1.4(3)	1.4(5)	0	$1/2^+$	984	100(16)	100
1698	$5/2^+$		1.15(20)	1.3(5)	0	$1/2^+$	1698	152(24)	100
1940	$5/2^+$		0.89(16)	$1.4(^{+6}_{-4})$	984	$3/2^+$	955	8.2(13)	50(6)
					0	$1/2^+$	1940	8.2(13)	50(6)
3109	$(7/2^+)$	0.103(30)	0.10(5)		1940	$5/2^+$	1169	5.0(8)	100
3427	$(5/2^+, 7/2^+)$	0.100(49)			1698	$5/2^+$	1729	13(2)	58(6)
					984	$3/2^+$	2442	9.0(15)	42(6)
3476	$1/2^+$	< 0.010			0	$1/2^+$	3476	11(2)	100
3561	$3/2^-$	< 0.010			0	$1/2^+$	3561	29(5)	100
3760	$5/2^-, 7/2^-$	0.58(13)	0.64(15)		1698	$5/2^+$	2062	88(15)	100
3787	$3/2^+$	< 0.024			1698	$5/2^+$	2088	6.0(9)	52(6)
					0	$1/2^+$	3787	5.5(8)	48(6)

Table 3.1: ^{27}Mg transitions and levels observed in the experiment. Data on new candidate transitions are not reported.
Energies and spin-parity values are taken from [1]; branching ratios and intensities, which are relative to the 984 keV transition, are measured in the experiment. Uncertainties are preliminary and include a 10% systematic error on the detector efficiency component, since a calibration from 2022 executed on a different configuration for AGATA was used to obtain it (fig 3.4).

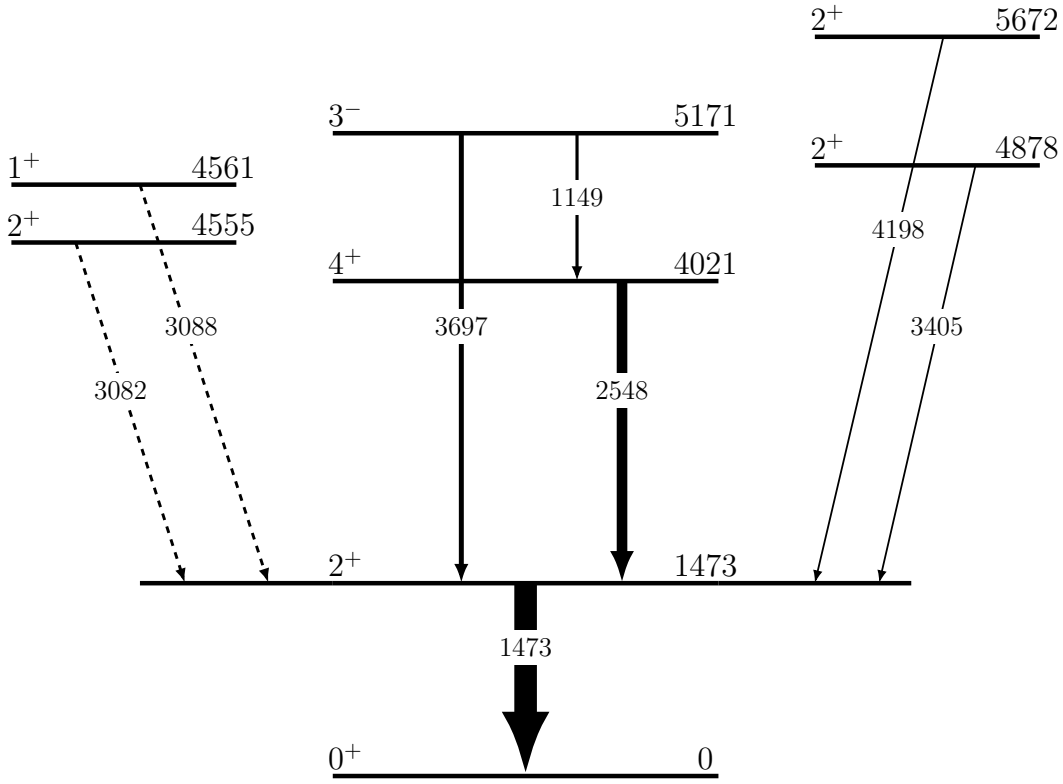

Figure 3.6: Reconstructed level scheme of ^{28}Mg.

Energy levels		Previous τ measurements		Transitions				
E_i keV	J_i^π	τ [14] ps	τ [15] ps	E_f keV	J_f^π	E_γ keV	I_γ %	Br %
1473	2^+	1.6(2)	> 1.5	0	0^+	1473	100(16)	100
4021	4^+	0.21(7)	0.18(3)	1473	2^+	2548	47(8)	100
4555	2^+		< 0.045	1473	2^+	3082	7.8(14)*	100
4561	1^+	< 0.04		1473	2^+	3088	7.8(14)*	100
4878	2^+	< 0.18	< 0.026	1473	2^+	3405	1.3(3)	100
5171	3^-	0.10(3)	$0.26(^{+16}_{-13})$	4021	4^+	1150	9.4(16)	39(6)
				1473	2^+	3698	15(3)	61(6)
5672	2^+		0.11(4)	1473	2^+	4198	1.7(4)	100

Table 3.2: ^{28}Mg transitions and levels observed in the experiment.
Energies and spin-parity values are taken from [1]; branching ratios and intensities, that are relative to the 1473 keV transition, are measured in the experiment. Uncertainties are preliminary and include a 10% systematic error on the detector efficiency component, since a calibration from 2022 executed on a different configuration for AGATA was used to obtain it (fig 3.4).
(*) Indistinguishable transitions that appear as a unique peak in the spectrum, the intensity collectively refers to this peak.

shifts resulting from the DSAM technique, make it impossible to distinguish between two possible transitions with very similar energies and the same exact final state, at least at the level of analysis conducted here. The red-colored arrow refers to the new candidate transition that was previously identified.

In tables 3.1 and 3.2 all results about identified levels and transitions are summarized. Lifetime measurements present in literature are also reported in order to help identifying which levels are feasible to be investigated in this work. Since the maximum sensitivity range of the experiment goes from 50 fs to 0.8 ps, an estimate of lifetime is being calculated for the following levels:

- in ^{27}Mg, the $(7/2^+)$ level at 3109 keV and the $(5/2^+, 7/2^+)$ state at 3427 keV;
- in ^{28}Mg, the first 4^+ at 4021 keV and the 3^- state at 5171 keV.

3.2 Monte Carlo simulations for lifetimes measurement

The extraction of lifetimes from the experimental energy spectrum is done via a line-shape comparison of transition peaks against model spectra obtained through Monte Carlo simulations. These have been conducted with the `GEANT4` toolkit, a powerful widely-used software for analyzing experiments in nuclear physics, that can simulate a variety of physical processes and handle complex detector geometry [25]. Basically, `GEANT4` allows to reproduce with random events all possible interactions and mechanisms that can take place in a reaction, respecting all physical properties of the particles involved. For the analysis conducted in this work, a code based on `GEANT4` and specifically designed for the Advanced Tracking Array and its ancillary devices, the AGATA simulation package [26], was used. This package offers an accurate emulation of both geometry and materials of AGATA detectors, allowing to select which crystals are present and where they are positioned with respect to beam and target.

Among all parameters that can be changed in the simulation code to reproduce experimental conditions at best, there are the resolution of detectors, their efficiency, population values of different energy levels, complex γ-ray cascades between levels, branching ratios, and obviously, lifetimes.

3.2.1 The line-shape analysis method

The procedure to get a measurement involves simulating a set of spectra by varying only one parameter, that is the lifetime of a specific state in this case, until the histogram that better matches experimental data is found. The quality of the comparison between experimental and simulated histograms is given by the least-χ^2 method, that is the minimization of the sum of squared residuals between the two datasets. The χ^2 quantity for a fit between two histograms is defined as follows:

$$\chi^2 = \sum_i \left(\frac{n_i^{\mathrm{exp}} - n_i^{\mathrm{sim}}}{\sigma^{\mathrm{exp}}} \right)^2 \tag{3.2}$$

where i is an index that varies among bins in the fit region, usually chosen to contain only the peak related to the transition of interest and small portions of background around it. n_i^{exp} is the number of counts in the i-th bin of the experimental histogram and n_i^{sim} is the equivalent for the simulation. σ_i^{exp} is the uncertainty on n_i^{exp}: since it is assumed that the experimental data follow a Poisson distribution, its value is equal to $\sigma^{\mathrm{exp}} = \sqrt{n^{\mathrm{exp}}}$.

The χ^2 formula does not consider an uncertainty on simulation values; these errors can be safely neglected if the number of simulated events sampled is sufficiently large so that statistical fluctuations that can affect the results are significantly reduced. For this reason, for each lifetime value 10^6 events have been simulated, in order to get samples containing 50 to 100 times the events in the experimental dataset (background excluded).

An additional discussion regarding the choice of the number of events in simulated datasets is proposed in appendix A. There, the χ^2 analysis for a single transition is repeated using simulations of different magnitudes, to get an insight on the impact of such variable on final results.

By calculating the χ^2 for different lifetime values, a characteristic curve is obtained. In correspondence with its minimum, the best lifetime estimate is found. The statistical uncertainty on this value for one sigma in the level of confidence is given by the region where $\Delta\chi^2 = \chi^2 - \chi^2_{\text{min}} = 1$. Systematic sources of error must be discussed and eventually added to this uncertainty in order to get the final estimate.

Line-shape fitting process and background addition

For a fixed lifetime, the process to get the simulated histogram for χ^2 evaluation against experimental data involves three main steps:

1. getting the peak shape by sampling gamma events with `GEANT4`;
2. estimating the background from experimental data and adding it to the simulated peak;
3. scaling the resulting histogram to match at best the experimental one.

It was chosen to estimate the background separately and not to generate it within `GEANT4` mainly for computational purposes, to speed up the production of simulated datasets and to reduce potential sources of error. The background is calculated for each transition by fitting an exponential function, $f_{\text{bg}}(E) = A \exp(-B \cdot E)$ with parameters A and B, on two narrow regions around the peak, respectively positioned on its left and right. These regions are selected to span at most a few hundreds keVs and not to include other identified peaks.

Once having both background $f_{\text{bg}}(E)$ and simulated peak from `GEANT4`, $h_{\text{sim}}(E_i;\tau)$, a new function is constructed:

$$F(s; E_i, \tau) = f_{\text{bg}}(E_i) + s \cdot h_{\text{sim}}(E_i;\tau) \tag{3.3}$$

This function is not continuous, as $h_{\text{sim}}(E_i;\tau)$ is a binned histogram evaluated only at certain energies E_i. The new variable s represents a scaling factor that serves to modify the peak-to-background ratio in the simulated histogram. The best estimate for this scaling factor is calculated by fitting the function $F(s; E_i, \tau)$ onto the experimental data. The final $F(\bar{s}; E_i, \tau)$, evaluated in correspondence of the best value of s, is the histogram used to obtain the χ^2 value for τ.

The energy range for $\bar{s}$ and χ^2 evaluation is defined case by case depending on the transition. In particular, for each peak analyzed two data samples are generated by imposing a 1 fs and a 10 ps lifetime, in order to get the maximum range in which the expected γ-ray events can lie. This range is the one selected for performing the various comparisons between simulations and experiment.

3.2.2 Optimization and characterization of simulations

Energy resolution of the detectors

A fundamental aspect that simulations must correctly reproduce is represented by the intrinsic energy resolution of AGATA detectors. Since the method earlier described is based on comparing line shapes, clearly simulated peaks need to have the same width as the experimental ones to avoid systematic errors that can negatively affect the analysis. To account for the finite, energy-varying detector resolution a smearing function has been added to the simulated data. It is defined for each event as

$$E_{\text{smeared}} = E_\gamma + \varepsilon(\mu = 0, \sigma_E) \qquad \sigma_E = \frac{\text{FWHM}(E_\gamma)}{2\sqrt{2\ln 2}} \tag{3.4}$$

where $\varepsilon(\mu = 0, \sigma_E)$ is a random number sampled from a Gaussian distribution centered at $\mu = 0$ with variance σ_E. FWHM(E_γ) represents the average response in FWHM of AGATA detectors as a function of energy. Without having at disposal any calibration data for the specific configuration adopted for AGATA and given that the spectra analyzed in this work still need to be refined, the best way to get the FWHM(E_γ) empirical trend is to use those exact spectra. Peaks referring to long-lived excited states, thus presumably having a small DSAM tail component, were selected among the ones previously identified, for both ^{27}Mg and ^{28}Mg. Their FWHMs, obtained through the fitting procedure described in 3.1, are plotted as a function of E_γ in figure 3.7.

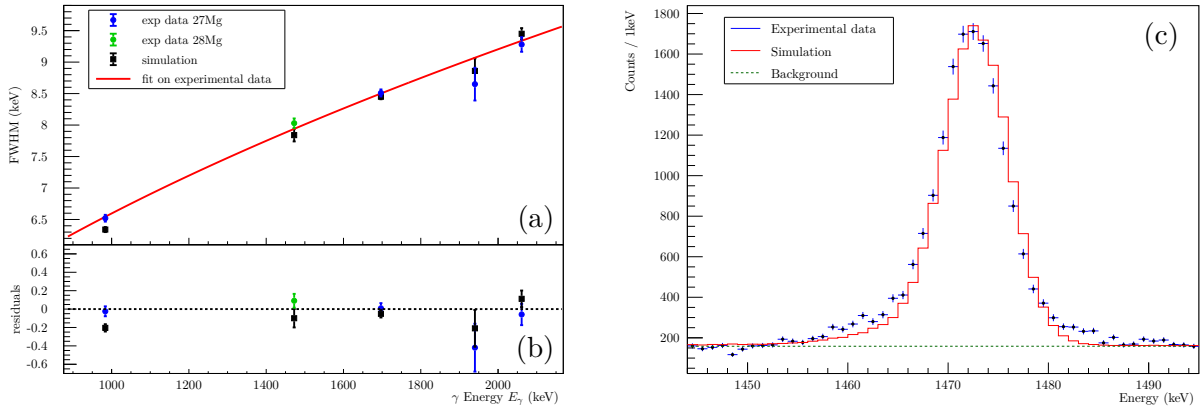

Figure 3.7: **(a)** Resolution of the detectors as a function of energy. Experimental data from ^{27}Mg and ^{28}Mg spectra, fitted with the 3.5 function. Comparison with the simulation adapted to the curve.
(b) Residuals of experimental and simulated FWHMs respect to the empirical trend.
(c) Example of simulation for the 1473 keV transition in ^{28}Mg. The FWHM is correctly reproduced. The experimental peak exhibits minor tails, especially on its right, that could not be simulated.

These data points were fitted with the following function, suggested in [24] to parameterize the response of HPGe detectors

$$\text{FWHM}(E_\gamma) = A + B \cdot \sqrt{\frac{E_\gamma}{1\ \text{MeV}}} \tag{3.5}$$

to obtain the empirical trend, at least within the interval of energies of the graph (going from 900 keV to 2200 keV). The χ^2 was minimized ($\chi^2_{\text{min}}/\text{ndf} = 4.5/3$) for the following values for A, B:

$$A = (0.3 \pm 0.2)\ \text{keV} \qquad B = (6.3 \pm 0.2)\ \text{keV}.$$

Such response function was implemented in the code and, as it can be seen from figure 3.7-(a), simulated peaks in the 900 keV to 2200 keV range have FWHMs comparable to the experimental ones. For transitions lying out of this energy range no data are available; and while the 3.5 equation could still be used, in order to get more reliable results the smearing process needs to be performed separately for each peak.

The gaussian smearing applied to the simulation does not include minor exponential tails that are present in experimental peaks (see figure 3.7-(b) for an example). Such tails could not be taken into account at this stage.

Range of sensitivity

The sensitivity to lifetime changes can be better investigated with the help of simulations. To get an insight into the range where precise lifetime measurements are possible a series of simulations were performed on the 1473 keV transition in ^{28}Mg. The state lifetime was changed within a wide range, going from 1 fs to 100 ps. To get the region where line-shape analysis is more effective, the ratio between the number of counts in the DC peak and the total number of events simulated (for normalization) was evaluated for each lifetime, as an index of sensitivity. In particular, the energy region referring to the DC peak was selected by observing the histograms for extreme τ values, as shown in figure 3.8-(a). The trend exhibited by the sensitivity index for varying lifetimes is plotted in figure 3.8-(b). As it can be seen, the 50 fs to 800 fs range is where such index varies most substantially, thus where DSAM is more effective in extracting lifetime measurements.

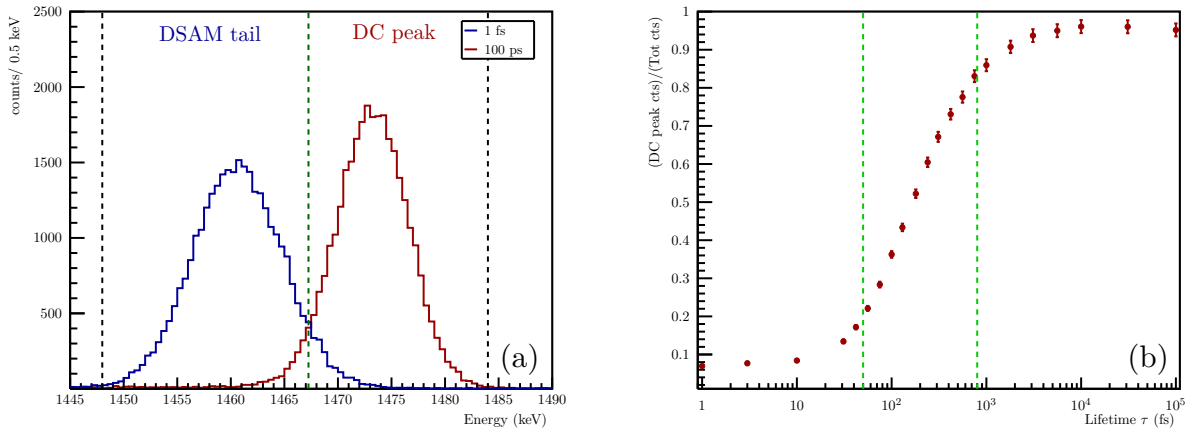

Figure 3.8: **(a)** Simulations for very small and large lifetimes at 1473 keV. Dashed lines show the identified energy regions for DC peak and DSAM tail.
(b) Trend of the the ratio between counts in DC peak and total events as a function of lifetime. Between dashed lines the range of maximum sensitivity, where the ratio varies the most for small changes in τ, is highlighted.

3.3 Lifetimes estimation

3.3.1 The 3109-keV level in ^{27}Mg

The 3109 keV level is located on top of the γ-ray cascade built above the first excited 984 keV state in ^{27}Mg. Previous measurements and shell model calculations expect it to be the lowest $7/2^+$ state for this nucleus, with a lifetime in the sensitive region of the DSAM technique. It is depopulated by only

one visible transition at 1169 keV and it was chosen because, despite the transition not being very intense, its lifetime is not influenced by side feeding from other levels.

Simulations were conducted in the range going from 90 to 200 fs, in steps of 10 fs. For each τ value the χ^2 was calculated following the method explained in section 3.2.1. The resulting curve is shown in figure 3.9-(b), where it has been fitted with a fourth-order polynomial to get its minimum, indicated by the red dashed line. Statistical uncertainty is obtained by the expression $\Delta\chi^2 = \chi^2 - \chi^2_{\text{min}}$ within one sigma in confidence level: this range is included between the two black dashed lines in 3.9-(b). In 3.9-(a) the simulation corresponding to the minimum χ^2 is represented against the experimental histogram. The dashed line is the estimated background added to the peak events obtained with `GEANT4`. The final estimate for the 3109 keV level lifetime with its statistical uncertainty is

$$\tau_{(3109\ \text{keV})} = (135^{+30}_{-25})\ \text{fs}.$$

The value of $\chi^2_{\text{min}} \approx 20.7$ is in line with expectations, being the number of degrees of freedom in the fit of ndf $= 17$. Also, the entity of statistical uncertainties given by the curve (relative error on τ of $\approx 20\%$) seems coherent, given the low intensity of the peak.

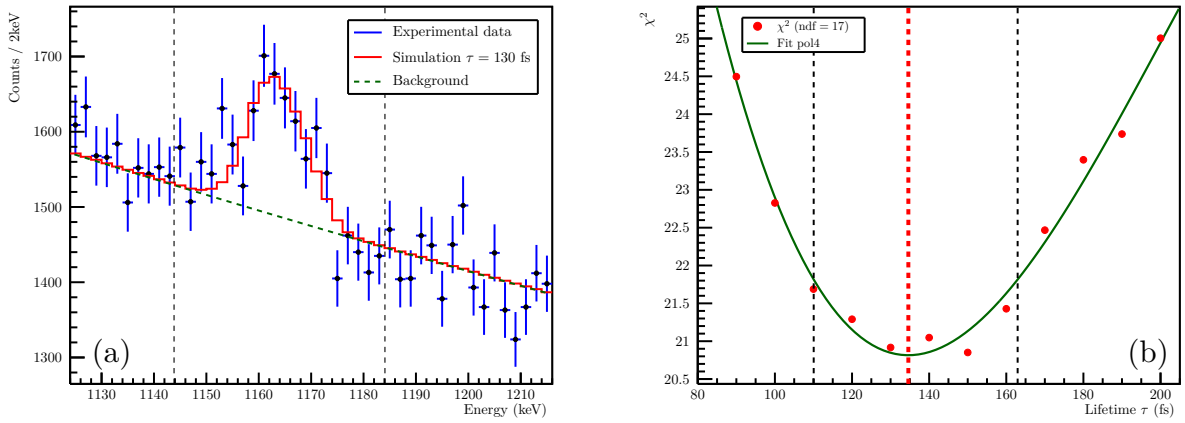

Figure 3.9: **(a)** Best simulated spectrum for the 1169 keV transition. The χ^2 analysis was performed in the $[1144 - 1184]$ keV interval, highlighted between two vertical lines.
(b) χ^2 curve fitted with a 4^{th} degree polynomial. The red line indicates the calculated minimum, while the black ones show the $\chi^2 - \chi^2_{\text{min}}$ range.

3.3.2 The 3427-keV level in ^{27}Mg

The 3427 keV level has similar characteristics to the one just analyzed: it is on the top of a γ-ray cascade, is only populated directly in the reaction, and has an expected lifetime lying in the DSAM range. It decays via two possible transitions with similar branching ratios: one that goes to the $5/2^+$ level at 1698 keV, the other going to the 984 keV state. The first one, despite being visible in the spectrum, is not suitable to be studied with the methodology presented here: its energy is too close to the most intense peak observed in ^{27}Mg, the one at 1698 keV. This makes it difficult to accurately estimate the relative intensity between the two peaks, that are correlated one to another, being part of the same cascade. For this reason, only the transition at 2442 keV has been analyzed. The lifetime of the level can be estimated from the one specifically relative to this transition by knowing its branching ratio.

Similarly to what was done in the previous case, simulations were performed every 10 fs in the 70−180 fs range. The results, with the χ^2 curve and the sample that better suits experimental data, are reported in figure 3.10. The lifetime obtained for this transition, without including systematic sources of error, is

$$\tau_{(\text{tr } 2442 \text{ keV})} = (118 \pm 9) \text{ fs}.$$

Also in this case, the results appear to be sufficiently significant, being the $\chi^2_{\text{min}} \approx 29$ equal to the number of degrees of freedom. The higher statistic in the experimental histogram results in a relative error on the estimate of only 8%.

The branching ratio for this transition obtained in section 3.1 by measuring peak intensities is $Br_{(\text{tr } 2442 \text{ keV})} = (50 \pm 6)\%$. With such value, the resulting lifetime for the 3427 keV level would be

$$\tau_{(3427 \text{ keV})} = Br_{(\text{tr } 2442 \text{ keV})} \cdot \tau_{(\text{tr } 2442 \text{ keV})} = (59 \pm 10) \text{ fs}. \tag{3.6}$$

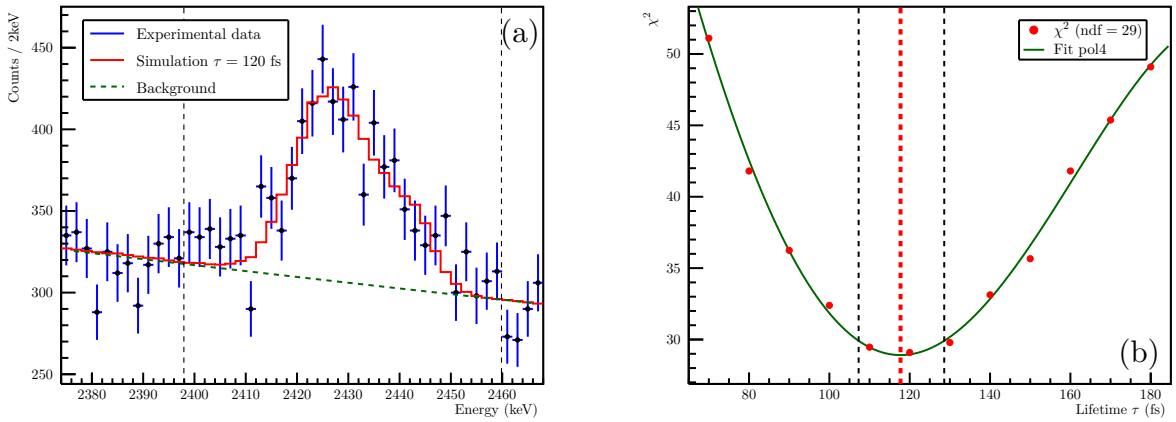

Figure 3.10: **(a)** Best simulated spectrum for the 2442 keV transition. The χ^2 analysis was performed in the $[2398 - 2460]$ keV interval, highlighted by two vertical lines.
(b) χ^2 curve fitted with a 4^{th} degree polynomial. The red line indicates the calculated minimum, while the black ones show the $\chi^2 - \chi^2_{\text{min}}$ range.

3.3.3 The 5171-keV level in ^{28}Mg

The 5171-keV level is the first negative parity state in ^{28}Mg. It is located on the top of the main γ cascade in the reconstructed level scheme for ^{28}Mg and is among the most populated states in the reaction. It is the initial level for two transitions that are both sufficiently intense and isolated from other peaks to be studied. With direct measurements of their characteristic lifetimes, both the level τ and the branching ratios for the two lines can be calculated.

The two transitions were simulated independently in `GEANT4`, removing entirely one of the two decay modes when generating samples for the other. For the most intense one, at 3969 keV, simulated datasets were produced with 10 fs steps, spanning the $100 - 190$ fs range (see figure 3.11-(c) and (d)). For the other transition, located at 1150 keV and expected to have a lower branching ratio, samples in the interval $200 - 700$ fs were generated, with larger 50 fs steps (fig 3.11-(a) and (b)). Table 3.3 resumes the results of such analysis.

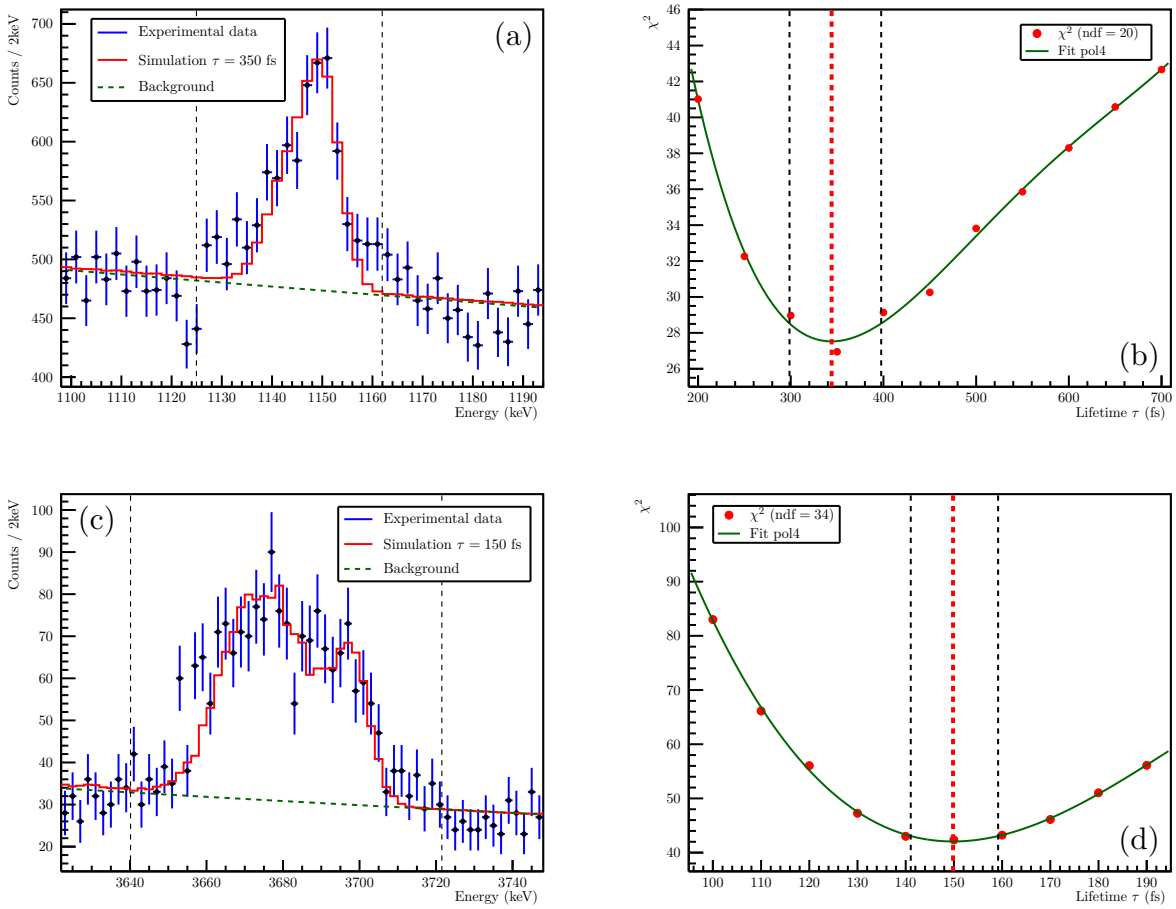

Figure 3.11: **(Top)** χ^2 analysis for the 1150 keV transition: χ^2 curve **(b)** and best sample obtained for minimum χ^2 **(a)**. Fits performed in the $[1125 - 1162]$ keV interval.
(Bottom) Same for the 3696 keV transition: χ^2 curve in **(d)** and best simulation in **(c)**. Fit interval $[3640 - 3722]$ keV.

E_i keV	J_i^π	E_f keV	J_f^π	E_γ keV	τ ps	$\chi^2_{\min}$ / ndf	Br (from τ) %	Br (from I) %
5171	3^-	4021	4^+	1150	$0.34(^{+6}_{-4})$	27.5 / 20	$31(^{+6}_{-4})$	39(6)
5171	3^-	1473	2^+	3698	0.150(9)	42.0 / 34	69(6)	61(6)

Table 3.3: Results for the two transitions coming from the 5171 keV state: lifetimes and branching ratios.

As it can be seen from the direct comparisons of the best-simulated samples with the experiment in figures 3.11-(a) and (c), some inconsistencies are evident, especially regarding the right minor tails of the experimental peaks that, as already addressed in 3.2.2, are not correctly reproduced by the simulation . However, in both cases, the minimum χ^2 is of the same order as the number of degrees of freedom in the fit, which can thus be considered sufficiently significant. Also, branching ratios extracted from the two lifetime values, reported in 3.3, are coherent with the first estimates obtained from the measurements of relative intensity executed in section 3.1. With the lifetimes for the two transitions, finally the one for the 5171 keV state could be evaluated, as

$$\tau_{(5171\ \text{keV})} = \left(\frac{1}{\tau(\text{tr } 1150\ \text{keV})} + \frac{1}{\tau(\text{tr } 3696\ \text{keV})} \right)^{-1} = (104 \pm 7)\ \text{fs}. \tag{3.7}$$

3.3.4 The 4021-keV level in ^{28}Mg

The 4021 keV state of ^{28}Mg is the lower 4^+ level for this nucleus and decays with only one transition to the 1473 keV first excited 2^+ state. The only previous measurement [14] of its lifetime is of $\tau = (0.21 \pm 0.07)$ ps, so perfectly inside the sensitivity range of this experiment. The determination of its lifetime is, however, not as immediate as the ones already obtained, since this level is populated not only directly in the reaction but also by side feeding of 1150 keV transitions coming from the 5171 keV state. The simulation must account for this effect to get accurate results: in particular, several new parameters need to be included, such as the feeder lifetime and the relative populations of levels.

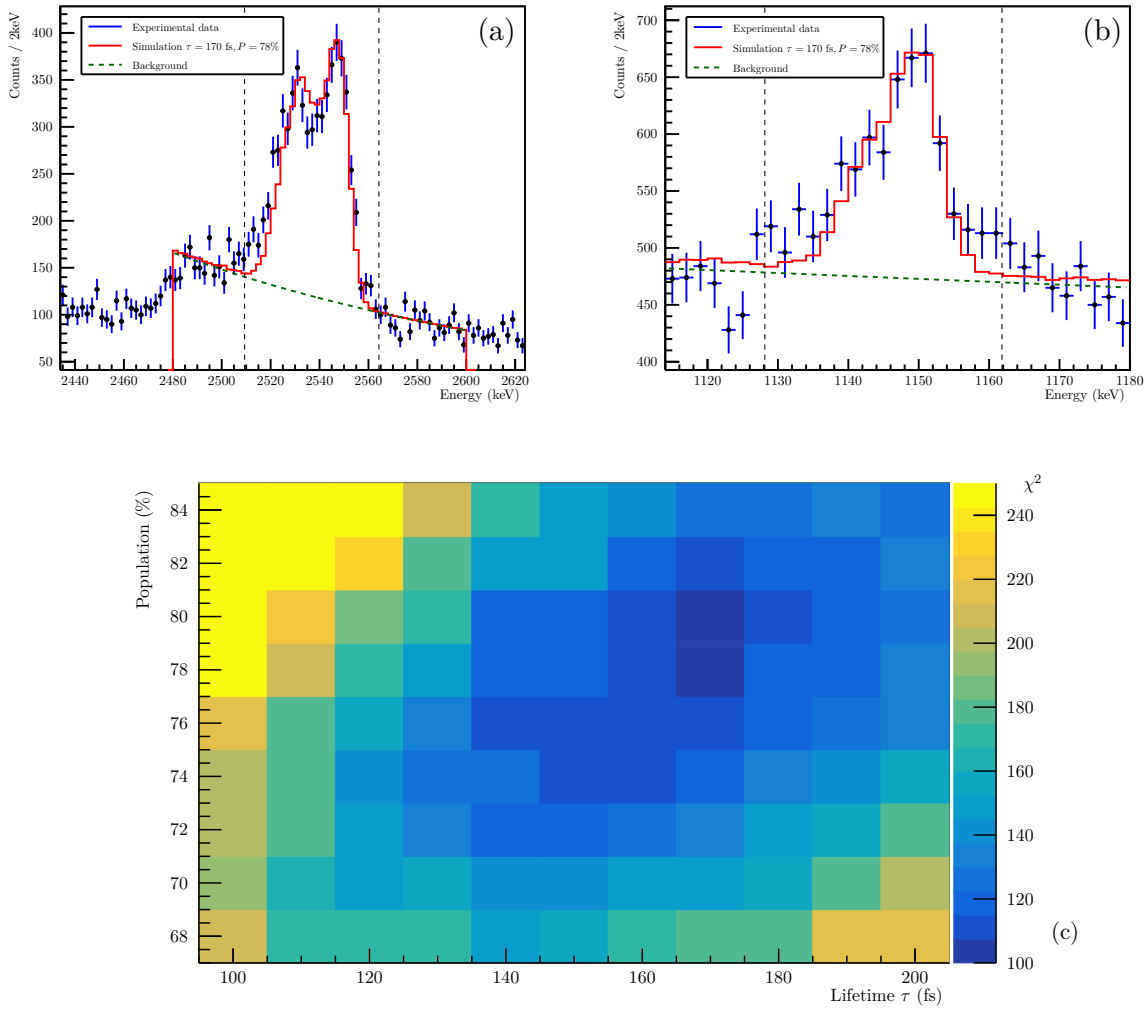

Figure 3.12: (a) and (b) Comparison of the best-simulated sample with experimental data, zoom on the 2548 keV peak in (a) and on the 1150 keV peak in (b). Fitting ranges highlighted between vertical lines: $[2508 - 2564]$ keV and $[1128 - 1162]$ keV.
(c) χ^2 distribution as a function of the 4021 keV state lifetime and of the relative population of such level. The points were fitted with a 4^{th} order polynomial surface to identify the global minimum.

To reduce the complexity, datasets were produced by simulating only partially the interested γ-ray cascade. In particular:

- three levels at 5171, 4021 and 1473 keV are included with two transitions, the main one, at 2547 keV from the 4021 level, and the feeder one, at 1150 keV from the higher 5171 state;

- the second transition coming from the 5171 state was not taken into account, to avoid the inclusion of branching ratios in the analysis;
- the lifetime of the feeding level was set to the value obtained in 3.3.3 specifically for the 1150 keV transition for all samples;
- only the 5171 and 4021 levels were populated. The relative percentage was left as a free parameter, together with the lifetime of the 4021 keV state.

So the χ^2 analysis was conducted on 2 free parameters in this case: samples were generated changing both the 4021 keV lifetime, within $[100 - 200]$ fs with steps of 10 fs, and the relative population of such level, within $[68, 84]\%$ by steps of 2% (the remaining percentage being the 5171 kev state population). Comparisons with experimental data for χ^2 evaluation are done simultaneously on two small energy ranges around the 1150 keV and the 2548 keV peak, with an analogous procedure to the one used for the previous cases (background estimation for each interval and simulation scaling).

In the end, a bi-dimensional χ^2 map is obtained (figure 3.12-(c)): in correspondence with its minimum, the best values for τ and relative population are found. Statistical uncertainties are given by the range that satisfies $\chi^2 - \chi^2_{\text{min}} < 2.3$, which corresponds to a confidence level of one standard deviation when evaluating 2 parameters at the same time. The values extracted from the map are:

$$\tau_{(4021\ \text{keV})} = (164 \pm 11)\ \text{fs} \qquad P_{4021} = (77.5 \pm 1.2)\%.$$

In this case the $\chi^2_{\text{min}} \approx 115$ is significantly higher than the expected number of degrees of freedom, which is 46. This fact affects the significance of the fit and is probably caused by the unidentified peak in the experimental data located around 2500 keV. Figure 3.13 shows the interested region: two possible exponential functions are depicted for the evaluation of the background, one that tries to include the contaminant (in red) and one obtained by excluding the whole $[2470, 2560]$ keV interval (in green).

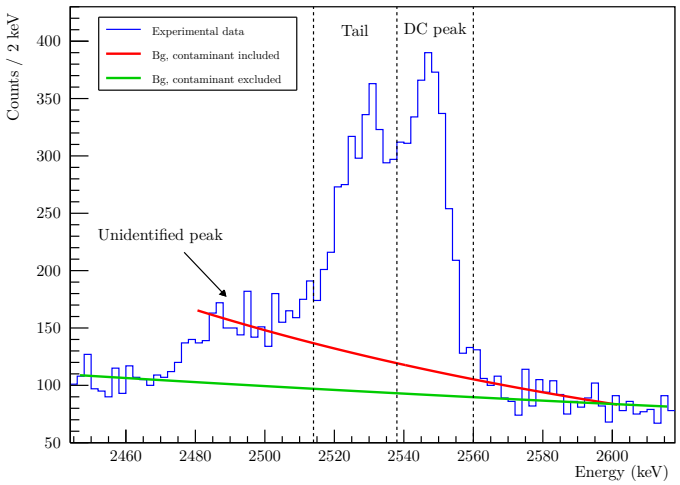

Figure 3.13: Region around the 2547 keV transition in ^{28}Mg. The unidentified peak on the transition left is evident. Two possible background functions are shown.

The analysis was conducted using the first background function, but such trend is probably inaccurate and a better solution would necessarily involve the identification of such peak. The recent work of Williams *et al.* [15], which studied the structure of ^{28}Mg with ^{12}C(^{18}O, 2p) fusion-evaporation reactions,

already observed the same exact anomaly, and suggested the existence of a new candidate transition of energy 2506.7(8) keV coming from a new state positioned at 6528.2(9) KeV. This claim followed after observing a coincidence with both the $2_1^+ \to 0_1^+$ and $4_1^+ \to 2_1^+$ transitions.

To address the impact of this possible new transition on the precision of the final measurement without directly including it in the analysis, an additional component of error must be added to the uncertainty. Such component is primarily evaluated with the aid of the sensitivity index introduced in section 3.2.2, that is the ratio between the number of counts in the DC peak and the total transition counts. As it can be seen from figure 3.8, such index is strongly related to the estimated transition lifetime: values in the $[0.2, 0.8]$ interval for the former are basically mapped to lifetimes in the wide $[50 - 800]$ fs region.

After having individuated the appropriate regions for the DC peak and the DSAM tail (see figure 3.13), this index is calculated twice, subtracting from the histogram either the background function that includes the contaminant peak (red) or the one that does not (green). All values are reported in table 3.4: the relative variation in the index between the two cases is of 27%. Hence, a systematic error of 27% is added in the $\tau_{(4021\text{ keV})}$ estimate due to the presence of the unidentified peak not reproduced in the simulation.

Background	Total cts	DC cts	Tail cts	DC/total ratio
contaminant included	957(84)	513(54)	444(63)	0.54(7)
contaminant excluded	2338(91)	959(63)	1379(70)	0.41(3)

Table 3.4: Number of counts for the 2547 keV transition: the tail region corresponds to $[2510, 2538]$ keV, while DC peak is in the interval $[2538, 2560]$ keV. Results calculated for different backgrounds (refer to fig 3.13).

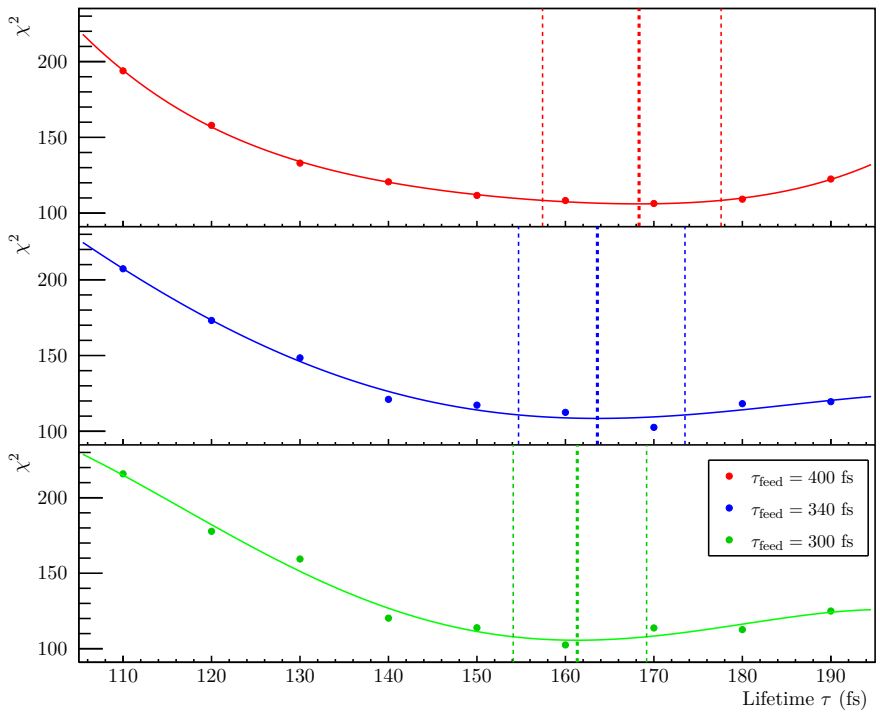

Figure 3.14: χ^2 curves referring to the 2548 keV transition of ^{28}Mg, obtained with different lifetimes for the feeder level and with relative population of 4021 keV state fixed at $P_{4021} = 77.5\%$. Minima of each curve are marked by thick dashed lines, while thinner lines indicate intervals where $\chi^2 - \chi^2_{\text{min}} < 2.3$, which correspond to the statistical uncertainties for a 2-parameter analysis, as the one executed on this transition.

Another limitation in the analysis just conducted is represented by the choice to fix the feeder transition lifetime. The value obtained for such quantity in section 3.3.3 was $\tau_{(tr\ 1150\ \mathrm{keV})} = (0.34^{+0.06}_{-0.04})$ ps. To understand the impact of this parameter on the 2548 keV peak shape, additional simulations have been performed, setting different values of $\tau_{(\mathrm{tr}\ 1150\ \mathrm{keV})}$. In particular, after fixing the 4021 keV level relative population, 3 sets of simulations were produced imposing $\tau_{(\mathrm{tr}\ 1150\ \mathrm{keV})} \in \{0.30, 0.34, 0.40\}$ ps respectively, to get the maximum variance of $\tau_{(4021\ \mathrm{keV})}$ when changing the feeder lifetime within a confidence level of one standard deviation. The results are shown in figure 3.14. A systematic trend is evident, as higher lifetimes for the feeder result in higher values also for the lower state lifetime. However, this effect appears to be less relevant than the correction needed for the presence of the contaminant peak, the relative variation between extremal χ^2 minima being of only 5%. Ultimately, a second component of systematic error of 5% is further added to the $\tau_{(4021\ \mathrm{keV})}$ estimate, to account for the fluctuations of the feeder lifetime. Including all sources of systematic error identified, the final estimate of the 4021 keV state becomes

$$\tau_{(4021\ \mathrm{keV})} = (164 \pm 11 \oplus 44 \oplus 8)\ \mathrm{fs} = (164 \pm 46)\ \mathrm{fs}$$

3.4 Discussion of the results

In table 3.5, lifetimes obtained for the selected excited states in ^{27}Mg and ^{28}Mg are summarized. Also measurements of these quantities coming from previous works are reported for a comparison: all such values were directly derived using the DSAM technique, with similar procedures as the ones applied here. The major difference with the present experiment lies in the nuclear reactions analyzed: the works of Brendler *et al.* in 1977 [11] and of Costa and Beck in 1972 [13] studied the structure of ^{27}Mg with $^{26}\mathrm{Mg}(\mathrm{d}, \mathrm{p}\gamma)$ reactions; the one by Fisher *et al.* in 1973 produced ^{28}Mg nuclei using a tritium beam on a ^{26}Mg target; finally, the more recent work of Williams *et al.* [15] populated ^{28}Mg excited levels in $^{12}\mathrm{C}(^{18}\mathrm{O}, 2\mathrm{p})$ fusion-evaporation reactions.

Nucleus	Energy level		Present work	Literature			
	E keV	J^π	τ ps	τ [11] ps	τ [13] ps	τ [14] ps	τ [15] ps
^{27}Mg	3109	$(7/2^+)$	$0.135(^{+30}_{-25})$	0.103(30)	0.10(5)		
^{27}Mg	3427	$(5/2^+, 7/2^+)$	0.059(10)	0.100(49)			
^{28}Mg	4021	4^+	0.164(46)			0.21(7)	0.18(3)
^{28}Mg	5171	3^-	0.104(7)			0.10(3)	$0.26(^{+16}_{-13})$

Table 3.5: Summary of ^{27}Mg and ^{28}Mg lifetimes estimated in this thesis. Precedent values present in literature are reported for a direct comparison.

The measurements obtained in this work are all sufficiently consistent and compatible with the ones present in the literature. In particular, no problematic trends, such as systematically over- or underestimated values, are to be noted, adding to the reliability of the procedure implemented. As regards the precision, the estimates calculated here exhibit an equal or better relative uncertainty respect to literature values. This is mainly due to the very large statistics that have been collected in the experiment: statistical uncertainties coming from χ^2 analysis of the selected transitions correspond to a $6 \div 22\%$ relative error on the lifetimes, which is significantly lower than the ones that could be obtained in the works cited before.

It is important to remind that the measurements proposed here come from the analysis of preliminary spectra, hence they must not be considered as definitive. Such precision values could reliably be improved by using the final experimental spectra, that will be available after the completion of a more in-depth analysis of raw data coming from AGATA+PRISMA. Still, these results show both the potential and the reliability of the methodologies and procedures proposed to extract lifetimes, procedures that can thus be safely implemented for the future systematic analysis that will be conducted on all states and channels populated in the reaction.

Chapter 4

Summary and conclusion

In this thesis, the lifetimes of four excited states in ^{27}Mg and ^{28}Mg have been measured using the Doppler Shift Attenuation Method (DSAM). Data produced in experiment 23.068 conducted in June 2024 at the Legnaro National Laboratories were analyzed, identifying visible known transitions and highlighting possible new γ-ray candidates. This experiment is the second of a three-step campaign, aimed at investigating the structure of nuclei in the region towards the Island of Inversion at $N = 20$. In the campaign, the products of multi-nucleon transfer reactions induced by neutron-rich stable beams (^{22}Ne in the first experiment, ^{26}Mg in the one analyzed here and ^{30}Si in the future one) onto ^{238}U targets are studied using the gamma ray tracking array AGATA coupled with the PRISMA magnetic spectrometer.

This work serves as an initial approach to validate the methodology used to measure lifetimes using DSAM in this experiment. The analysis method implemented was based on direct line-shape comparisons between experimental data and sets of spectra generated with realistic `GEANT4` Monte Carlo simulations. The steps needed to adapt the simulation to match the experimental conditions and better emulate the observed histograms have been discussed thoroughly, as well as the possible sources of error that could affect final measurements. Overall, the simulation refinement work proposed in the thesis has produced accurate results. The lifetimes obtained for the selected levels, despite being only preliminary estimates, are compatible within the uncertainties with the values present in literature. Their precision is comparable or better than the one of previous measurements. This was made possible by the beam quality provided by the LNL accelerators, the advanced tracking capabilities of AGATA, and the high acceptance of PRISMA, factors that allowed for the collection of a large amount of data with excellent resolution.

After the completion of the pre-processing of raw experimental data from AGATA+PRISMA, the extraction of lifetimes may be conducted more systematically on all identified levels and nuclei, by following similar procedures to the one applied in this work. Those values will then serve for a comparative analysis with the literature and, most importantly, with theoretical shell model calculations, to achieve a better understanding on shell evolution and nuclear structures in the isotopes near the Island of Inversion. Of particular physical importance, among all the channels populated in the reaction, there are for example the negative parity states in Mg isotopes, especially in odd-even ^{29}Mg and ^{27}Mg, as they can be used to infer the *sd-fp* shell-gap magnitude and are expected to help in obtaining a clearer description of the transition to the Island of Inversion from the $Z = 12$ chain.

Appendix A

Number of events in simulated datasets

As observed within the explanation of the line-shape comparison method, χ^2 values for evaluating the goodness of a fit do not include an error on simulated data. Simulations are subject statistical fluctuations, that can be reduced by producing bigger samples. To test eventual variations caused by choosing a different number of events, the analysis on the 2442 keV transition in ^{27}Mg has been repeated using samples of $0.5 \cdot 10^6$ and $2.5 \cdot 10^6$ events, in addition to the ones of $1.0 \cdot 10^6$ events already used in section 3.3.2. The χ^2 curves resulting from the 3 sets of samples are compared in figure A.1. No significant differences are to be seen between them: they provide very similar values for the lifetime and its statistical uncertainty. However, already using only half a million events per sample leads to evident oscillations between different points in the curve. 10^6 events on the other hand were estimated to be enough for obtaining sufficiently smooth χ^2 curves.

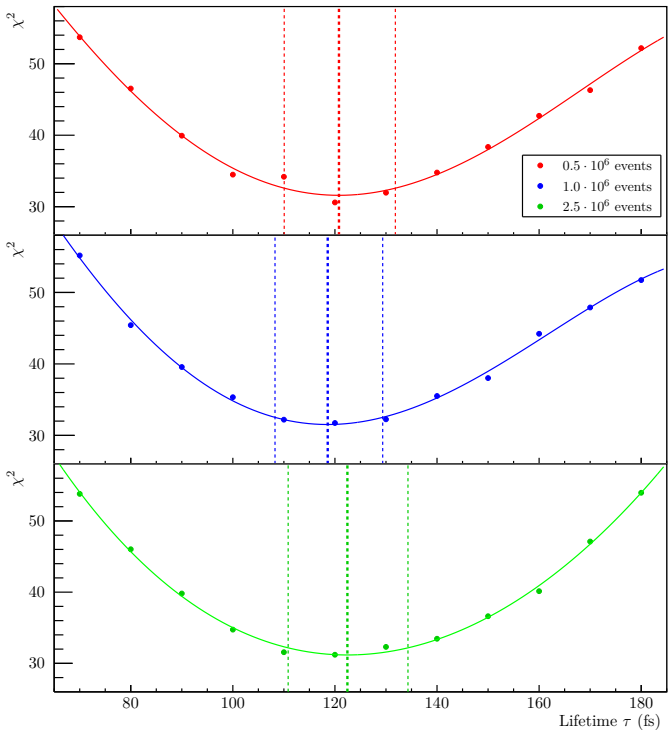

Figure A.1: χ^2 curves referring to the 2442 keV transition of ^{27}Mg, obtained with simulated samples of different sizes. Dashed lines show the minimum of each curve and the interval associated with one sigma in confidence level, defined by $\chi^2 - \chi^2_{\text{min}} < 1$.

Bibliography

[1] 'National nuclear data center, information extracted from the nudat database.' (2024), [Online]. Available: https://www.nndc.bnl.gov/.

[2] M. G. Mayer, 'On closed shells in nuclei. ii,' *Phys. Rev.*, vol. 75, pp. 1969–1970, 12 Jun. 1949. DOI: 10.1103/PhysRev.75.1969. [Online]. Available: https://link.aps.org/doi/10.1103/PhysRev.75.1969.

[3] O. Haxel, J. H. D. Jensen and H. E. Suess, 'On the "magic numbers" in nuclear structure,' *Phys. Rev.*, vol. 75, pp. 1766–1766, 11 Jun. 1949. DOI: 10.1103/PhysRev.75.1766.2. [Online]. Available: https://link.aps.org/doi/10.1103/PhysRev.75.1766.2.

[4] K. Krane, *Introductory Nuclear Physics*. Wiley, 1991, ISBN: 9780471805533. [Online]. Available: https://books.google.it/books?id=BNtVEAAAQBAJ.

[5] E. Caurier, G. Martínez-Pinedo, F. Nowacki, A. Poves and A. P. Zuker, 'The shell model as a unified view of nuclear structure,' *Reviews of Modern Physics*, vol. 77, no. 2, pp. 427–488, Jun. 2005, ISSN: 1539-0756. DOI: 10.1103/revmodphys.77.427. [Online]. Available: http://dx.doi.org/10.1103/RevModPhys.77.427.

[6] N. Tsunoda *et al.*, 'The impact of nuclear shape on the emergence of the neutron dripline,' *Nature*, vol. 587, pp. 66–71, 2020. DOI: https://doi.org/10.1038/s41586-020-2848-x.

[7] E. Caurier, F. Nowacki and A. Poves, 'Merging of the islands of inversion at $N = 20$ and $N = 28$,' *Phys. Rev. C*, vol. 90, p. 014 302, 1 Jul. 2014. DOI: 10.1103/PhysRevC.90.014302. [Online]. Available: https://link.aps.org/doi/10.1103/PhysRevC.90.014302.

[8] E. K. Warburton, J. A. Becker and B. A. Brown, 'Mass systematics for a=29–44 nuclei: The deformed a∼32 region,' *Phys. Rev. C*, vol. 41, pp. 1147–1166, 3 Mar. 1990. DOI: 10.1103/PhysRevC.41.1147. [Online]. Available: https://link.aps.org/doi/10.1103/PhysRevC.41.1147.

[9] A. Stefanini *et al.*, 'The heavy-ion magnetic spectrometer prisma,' *Nuclear Physics A*, vol. 701, no. 1, pp. 217–221, 2002, 5th International Conference on Radioactive Nuclear Beams, ISSN: 0375-9474. DOI: https://doi.org/10.1016/S0375-9474(01)01578-0. [Online]. Available: https://www.sciencedirect.com/science/article/pii/S0375947401015780.

[10] S. Akkoyun *et al.*, 'Agata—advanced gamma tracking array,' *Nuclear Instruments and Methods in Physics Research Section A: Accelerators, Spectrometers, Detectors and Associated Equipment*, vol. 668, pp. 26–58, 2012, ISSN: 0168-9002. DOI: https://doi.org/10.1016/j.nima.2011.11.081. [Online]. Available: https://www.sciencedirect.com/science/article/pii/S0168900211021516.

[11] W. Brendler, P. Betz, E. Bitterwolf and H. Röpke, 'The structure of ^{27}Mg from the ^{26}Mg(d, pγ) reaction,' *Zeitschrift für Physik A: Atoms and Nuclei*, vol. 281, no. 1–2, pp. 75–88, Mar. 1977,

ISSN: 1434-601X. DOI: 10.1007/bf01408616. [Online]. Available: http://dx.doi.org/10.1007/BF01408616.

[12] L. C. McIntyre, P. L. Carson and D. L. Barker, 'Mean lives of states in Mg^{27},' *Phys. Rev.*, vol. 184, pp. 1105–1111, 4 Aug. 1969. DOI: 10.1103/PhysRev.184.1105. [Online]. Available: https://link.aps.org/doi/10.1103/PhysRev.184.1105.

[13] G. Costa and F. Beck, 'Mesures de vies moyennes et de coefficients de mélange dans le noyau 27mg,' *Nuclear Physics A*, vol. 181, no. 1, pp. 132–144, 1972, ISSN: 0375-9474. DOI: https://doi.org/10.1016/0375-9474(72)90906-2. [Online]. Available: https://www.sciencedirect.com/science/article/pii/0375947472909062.

[14] T. R. Fisher *et al.*, 'Gamma-ray spectroscopy of low-lying levels in ^{28}Mg,' *Phys. Rev. C*, vol. 7, pp. 1878–1885, 5 May 1973. DOI: 10.1103/PhysRevC.7.1878. [Online]. Available: https://link.aps.org/doi/10.1103/PhysRevC.7.1878.

[15] J. Williams *et al.*, 'Structure of ^{28}Mg and influence of the neutron *pf* shell,' *Phys. Rev. C*, vol. 100, p. 014 322, 1 Jul. 2019. DOI: 10.1103/PhysRevC.100.014322. [Online]. Available: https://link.aps.org/doi/10.1103/PhysRevC.100.014322.

[16] G. Montagnoli *et al.*, 'The large-area micro-channel plate entrance detector of the heavy-ion magnetic spectrometer prisma,' *Nuclear Instruments and Methods in Physics Research Section A: Accelerators, Spectrometers, Detectors and Associated Equipment*, vol. 547, no. 2, pp. 455–463, 2005, ISSN: 0168-9002. DOI: https://doi.org/10.1016/j.nima.2005.03.158. [Online]. Available: https://www.sciencedirect.com/science/article/pii/S0168900205009241.

[17] S. Beghini *et al.*, 'The focal plane detector of the magnetic spectrometer prisma,' *Nuclear Instruments and Methods in Physics Research Section A: Accelerators, Spectrometers, Detectors and Associated Equipment*, vol. 551, no. 2, pp. 364–374, 2005, ISSN: 0168-9002. DOI: https://doi.org/10.1016/j.nima.2005.06.058. [Online]. Available: https://www.sciencedirect.com/science/article/pii/S0168900205013501.

[18] R. Nicolas del Aramo, 'Study of lifetimes of nuclear excited states near the n=20 island of inversion using the doppler shift attenuation method,' M.S. thesis, Università degli Studi di Padova, 2022. [Online]. Available: https://hdl.handle.net/20.500.12608/51899.

[19] J. Valiente-Dobón *et al.*, 'Conceptual design of the agata 2π array at lnl,' *Nuclear Instruments and Methods in Physics Research Section A: Accelerators, Spectrometers, Detectors and Associated Equipment*, vol. 1049, p. 168 040, 2023, ISSN: 0168-9002. DOI: https://doi.org/10.1016/j.nima.2023.168040. [Online]. Available: https://www.sciencedirect.com/science/article/pii/S016890022300030X.

[20] A. Lopez-Martens, K. Hauschild, A. Korichi, J. Roccaz and J.-P. Thibaud, 'Gamma-ray tracking algorithms: A comparison,' *Nuclear Instruments and Methods in Physics Research Section A: Accelerators, Spectrometers, Detectors and Associated Equipment*, vol. 533, no. 3, pp. 454–466, 2004, ISSN: 0168-9002. DOI: https://doi.org/10.1016/j.nima.2004.06.154. [Online]. Available: https://www.sciencedirect.com/science/article/pii/S0168900204014779.

[21] O. B. Tarasov and D. Bazin, 'Lise++: Radioactive beam production with in-flight separators,' *Nuclear Instruments and Methods in Physics Research Section B: Beam Interactions with Materials and Atoms*, vol. 266, no. 19-20, pp. 4657–4664, 2008.

[22] S. Hinds, H. Marchant and R. Middleton, 'The energy levels of the magnesium isotopes of mass 25 to 28,' *Proceedings of the Physical Society*, vol. 78, no. 4, p. 473, Oct. 1961. DOI: 10.1088/0370-1328/78/4/301. [Online]. Available: https://dx.doi.org/10.1088/0370-1328/78/4/301.

[23] R. P. Vidal *et al.*, 'Agata performance ii: Efficiency and p/t,' *LNL Annual Report 2022*, vol. 1049, pp. 56–57, 2023, ISSN: 1828-8561. [Online]. Available: https://web.infn.it/internal_report-LNL/annual-report/.

[24] D. Radford, 'Escl8r and levit8r: Software for interactive graphical analysis of hpge coincidence data sets,' *Nuclear Instruments and Methods in Physics Research Section A: Accelerators, Spectrometers, Detectors and Associated Equipment*, vol. 361, no. 1, pp. 297–305, 1995, ISSN: 0168-9002. DOI: https://doi.org/10.1016/0168-9002(95)00183-2. [Online]. Available: https://www.sciencedirect.com/science/article/pii/0168900295001832.

[25] S. Agostinelli *et al.*, 'Geant4—a simulation toolkit,' *Nuclear Instruments and Methods in Physics Research Section A: Accelerators, Spectrometers, Detectors and Associated Equipment*, vol. 506, no. 3, pp. 250–303, 2003, ISSN: 0168-9002. DOI: https://doi.org/10.1016/S0168-9002(03)01368-8. [Online]. Available: https://www.sciencedirect.com/science/article/pii/S0168900203013688.

[26] E. Farnea *et al.*, 'Conceptual design and monte carlo simulations of the agata array,' *Nuclear Instruments and Methods in Physics Research Section A: Accelerators, Spectrometers, Detectors and Associated Equipment*, vol. 621, no. 1, pp. 331–343, 2010, ISSN: 0168-9002. DOI: https://doi.org/10.1016/j.nima.2010.04.043. [Online]. Available: https://www.sciencedirect.com/science/article/pii/S0168900210008922.